



## Tectonics

### RESEARCH ARTICLE

10.1029/2018TC005132

#### Key Points:

- New thermochronologic ages provide a detailed chronology of deformation in the central Andean retroarc of southern Bolivia
- Sequential cross-section restoration elucidates Cenozoic rates of crustal shortening, thrust front propagation, and orogenic wedge evolution
- Modulation of upper-plate deformation and surface uplift in the central Andes is tied to build up and foundering of an eclogitic root

#### Supporting Information:

- Supporting Information S1
- Data Set S1
- Data Set S2

#### Correspondence to:

R. B. Anderson,  
ryan.b.anderson@wsu.edu

#### Citation:

Anderson, R. B., Long, S. P., Horton, B. K., Thomson, S. N., Calle, A. Z., & Stockli, D. F. (2018). Orogenic wedge evolution of the central Andes, Bolivia (21°S): Implications for Cordilleran cyclicity. *Tectonics*, 37. <https://doi.org/10.1029/2018TC005132>

Received 5 MAY 2018

Accepted 16 AUG 2018

Accepted article online 28 AUG 2018

## Orogenic Wedge Evolution of the Central Andes, Bolivia (21°S): Implications for Cordilleran Cyclicity

R. B. Anderson<sup>1</sup> , S. P. Long<sup>1</sup> , B. K. Horton<sup>2,3</sup> , S. N. Thomson<sup>4</sup>, A. Z. Calle<sup>2,3</sup>, and D. F. Stockli<sup>2</sup> 

<sup>1</sup>School of the Environment, Washington State University, Pullman, WA, USA, <sup>2</sup>Department of Geological Sciences, Jackson School of Geosciences, University of Texas at Austin, Austin, TX, USA, <sup>3</sup>Institute for Geophysics, Jackson School of Geosciences, University of Texas at Austin, Austin, TX, USA, <sup>4</sup>Department of Geosciences, University of Arizona, Tucson, AZ, USA

**Abstract** The Andes are an ideal setting to explore orogenic wedge evolution and the cyclical tectonic processes in Cordilleran convergent-margin systems. Paleoelevation data suggest that the hinterland plateau in southern Bolivia underwent rapid surface uplift at ~16–9 Ma, which is predicted to have induced rapid thrust belt propagation. We integrate fission track and (U-Th)/He ages from zircon and apatite with a sequentially restored cross section to quantify the timing and rates of thrust belt propagation in southern Bolivia for the last ~43 Myr. These data show that retroarc shortening in the Eastern Cordillera propagated westward from ~43 to 27 Ma as the wedge grew to attain critical taper and steady state. The thrust front then advanced rapidly eastward from ~25 to 17 Ma across the western Interandean zone, where a weak decollement modified the critical taper angle. The thrust front stalled for ~6 Myr but resumed eastward advance into the eastern Interandean zone and Subandean zone by ~11–8 Ma, which we interpret as a response to increased accretionary influx and rapid orogenic wedge expansion induced by eclogitic delamination and corresponding hinterland surface uplift at ~13 Ma. Development of an orographic barrier and wetter climatic conditions resulted in relatively steady state wedge conditions from ~8.5 to 1.5 Ma. Rapid wedge growth after ~1.5 Ma may be attributed to mass accumulation in the orogen interior or a weakened decollement. Our data reveal space-time variations in orogenic wedge evolution consistent with models of Cordilleran cyclicity and lithospheric removal, with important additional influences of erosion, climate, and rock rheology.

### 1. Introduction

Crustal shortening of the overriding continental plate in Cordilleran orogenic systems is invariably linked to the degree of mechanical coupling with the subducting oceanic plate (e.g., Coney & Evenchick, 1994; Dewey & Bird, 1970; Horton, 2018a; Jordan et al., 1983; Maloney et al., 2013; Schellart, 2008). Absolute plate velocity and subducting slab geometry likely regulate the tectonic mode of the upper plate in a Cordilleran system (e.g., contraction, extension, or neutral; Horton, 2018a; Ramos, 2009), but the linkage between fluctuating rates of retroarc deformation and subduction-related kinematic parameters in the southern central Andes are often unclear (e.g., DeCelles et al., 2015; Oncken et al., 2006). However, recent geodynamic models also emphasize the important role that upper-plate processes play in controlling the overall evolution of such orogens (e.g., DeCelles et al., 2009; Ducea et al., 2013). The mechanical behavior of a fold-thrust belt is commonly described as an evolving wedge that deforms to maintain a critical taper angle (Buiter, 2012; Dahlen, 1990; Dahlen & Suppe, 1988; Davis et al., 1983; Platt, 1986). In this regard, the space-time patterns of thrust belt development can primarily be explained as responses to factors that influence or alter the taper of the orogenic wedge (e.g., DeCelles & Mitra, 1995), such as changes to the frictional resistance of the basal décollement (e.g., Davis et al., 1983; Wojtal & Mitra, 1986), changes in preexisting basin geometry or basement architecture (Allmendinger et al., 1983; Boyer, 1995), erosional modification and climatic variation (e.g., Dahlen, 1990; Horton, 1999; McQuarrie, Ehlers, et al., 2008; Willet, 1999), and the buildup and removal of dense lower lithosphere (e.g., DeCelles et al., 2009; Garzione et al., 2006; Wells et al., 2012).

The Cordilleran cyclicity model, which is rooted in critical taper theory, posits that several first-order processes operating within the continental plate (e.g., arc magmatism, rates of crustal shortening, foreland basin sedimentation, surface uplift, and the buildup and removal of eclogite bodies) are all linked by cause-effect relationships that occur in a temporal sequence over an ~25- to 50-Myr period (DeCelles et al., 2009, 2015;

DeCelles & Graham, 2015). In particular, accumulation and removal of eclogite bodies under the magmatic arc or hinterland (e.g., Ducea, 2002; Ducea et al., 2015; Krystopowicz & Currie, 2013; Saleeby et al., 2003) is interpreted to exert a strong control on the dynamics of the entire orogen. Removal of a dense root should induce a rapid isostatic increase in hinterland surface elevation (Currie et al., 2015; Garzione et al., 2008; Molnar et al., 1993) and/or create space for renewed underthrusting of material into the orogen (DeCelles et al., 2009; McQuarrie et al., 2005). If surface uplift sufficiently increases gravitational potential energy, or if renewed underthrusting perturbs the material flux balance by increasing the accretion rate, the frontal thrust belt is predicted to respond through an increase in forward propagation rate in order to restore an equilibrium surface slope (e.g., Dahlen, 1984; Garzione et al., 2006; Mourgues et al., 2014; Whipple & Meade, 2006). However, consequent changes in relief are related directly to erosion rates, and the growth of topography may also indirectly influence erosional flux by potentially altering the regional climate (e.g., Horton, 1999; McQuarrie, Ehlers, et al., 2008; Whipple, 2009; Willett, 1999). Furthermore, inherited features such as decollement strength and basin architecture may influence thrust belt propagation by changing the critical taper angle, which would perturb the accretionary material influx rate (Dahlen, 1990). Thus, studies that document the timing and rates of deformation, as well as characterize the factors that may influence this deformation, are necessary to enhance our understanding of geodynamic models such as critical taper and Cordilleran cyclicity (DeCelles et al., 2009; Whipple, 2009).

The central Andes have emerged as a focal point for debates over the processes affecting Cordilleran systems and the growth of orogenic plateaus (DeCelles et al., 2015; Garzione et al., 2017). In the southern Altiplano in Bolivia, isotopic and fossil data suggest that a rapid, ~2.5-km rise in hinterland surface elevation occurred between ~16 and ~9 Ma (Cadena et al., 2015; Garzione et al., 2014; Gregory-Wodzicki et al., 1998). This surface uplift event has been attributed to multiple processes, including removal of eclogitic lithosphere (Garzione et al., 2008; Hoke et al., 2007; Hoke & Garzione, 2008; Molnar & Garzione, 2007), ablative subduction of mantle lithosphere (Pope & Willett, 1998), and lower crustal flow from overthickened regions (Husson & Sempere, 2003). However, geochemical and isotopic data from lavas in southern Bolivia (Kay & Coira, 2009), geophysical data showing a lack of mafic lower crust (Beck & Zandt, 2002; Myers et al., 1998; Ryan et al., 2016), and mass balance calculations that suggest missing crustal area (Anderson et al., 2017; Eichelberger & McQuarrie, 2015; McQuarrie, 2002) all support the eclogitic removal scenario between ~20°S and 22°S (Garzione et al., 2017).

Rapid surface uplift and loss of an eclogitic root are predicted to have promoted wedge conditions that resulted in rapid forward propagation of the thrust front (e.g., Garzione et al., 2006, 2008). However, the timing and rates of shortening and thrust front propagation in southern Bolivia (before, during, and after rapid surface uplift) have not been determined with enough resolution to convincingly demonstrate a temporal link between surface uplift and thrust belt evolution, and the deformation timing within several key portions of the thrust belt remains debated (e.g., Barnes & Ehlers, 2009; Calle et al., 2018; Echavarría et al., 2003; Elger et al., 2005; Gubbels et al., 1993; Isacks, 1988; Lamb & Hoke, 1997; Sempere et al., 1997; Uba et al., 2009). In this study, we address this problem by focusing our efforts along a well-characterized transect across the Andean thrust belt at ~21°S, where published cross sections constrain the geometry and magnitude of shortening (Anderson et al., 2017; Elger et al., 2005). New and published thermochronologic ages are used to constrain the timing of thrust-related cooling, and to construct a ~43-Myr history of deformation at this latitude. These new timing constraints are integrated with forward modeling of thrust belt deformation, which allow us to quantify records of shortening rates and thrust front propagation rates. This facilitates comparison to the timing of events proposed to have influenced thrust belt evolution, most importantly the late Miocene rapid hinterland surface uplift event (Garzione et al., 2014; Gregory-Wodzicki et al., 1998).

## 2. Geologic Setting

Subduction of the Nazca plate beneath the South American plate has driven the Late Cretaceous-Cenozoic construction of the Andean orogen (e.g., Allmendinger et al., 1997; Coney & Evenchick, 1994; Isacks, 1988; Russo & Silver, 1996). In the central Andes (~16–24°S), development of the mountain belt has been characterized by formation of a volcanic arc along the western margin of the continent, eastward migration of a retro-arc fold-thrust belt and foreland basin system, and crustal thickening accompanied by topographic growth (DeCelles & Horton, 2003; Horton, 2005; Horton & DeCelles, 1997; Lamb & Hoke, 1997; McQuarrie et al., 2005; Sempere et al., 1997). Between these latitudes, the mountain belt reaches its maximum width

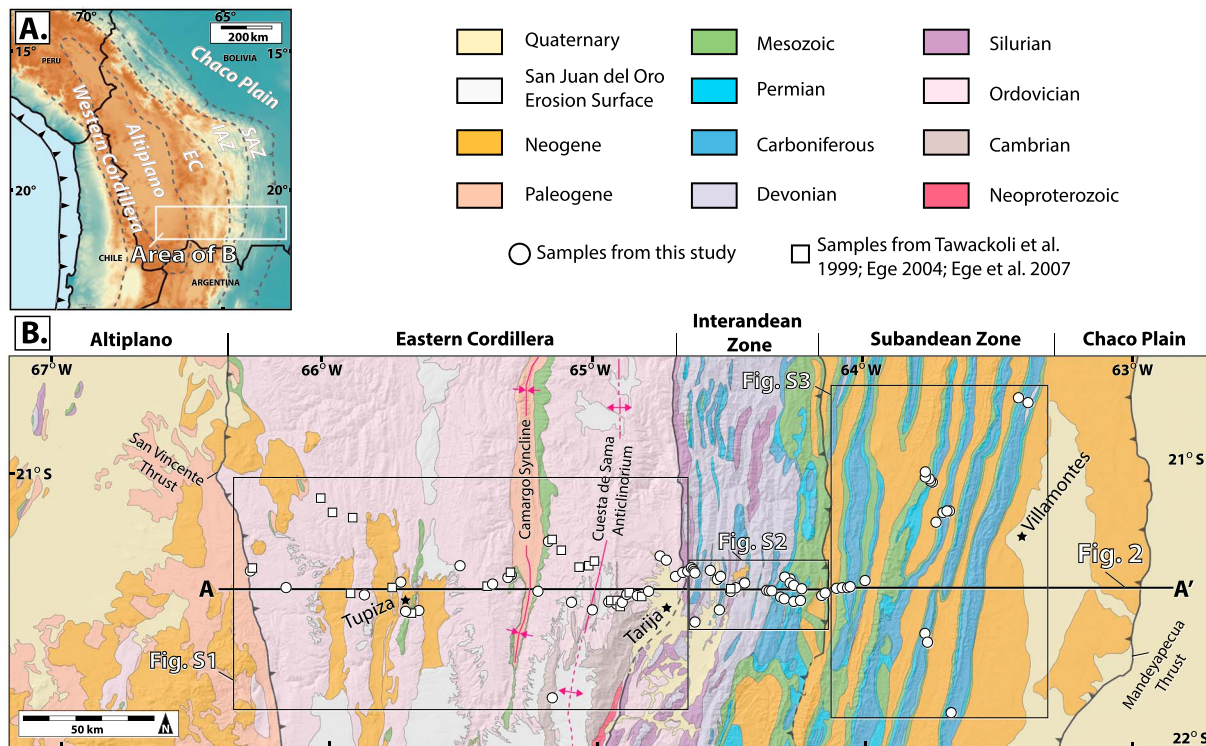


**Figure 1.** (a) Generalized geologic map of the retroarc thrust belt of southern Bolivia (~21–22°S; after Anderson et al., 2017; Servicio Nacional de Geología y Minería (SERGEOMIN), 2003) with locations of thermochronometry samples shown. Locations of geologic maps in the SI that show individual sample numbers (Figures S1–S3) are denoted by boxes. The bold line A–A' marks location of the cross section in Figure 2. (b) Topography of the central Andes (constructed from a Shuttle Radar Topography Mission 90-m digital elevation model); dashed gray lines mark the boundaries of Andean tectonomorphic zones.

(~500 km), total shortening in the fold-thrust belt is greatest (>300 km; e.g., Anderson et al., 2017; Arriagada et al., 2008; Eichelberger & McQuarrie, 2015; McQuarrie, 2002), and crustal thickness is on the order of 60–75 km (Beck & Zandt, 2002; Ryan et al., 2016).

The central Andean fold-thrust belt has been divided into distinct tectonomorphic zones based on major changes in topographic and structural elevation (Kley, 1996; McQuarrie, 2002). From west to east, these divisions include the Altiplano, Eastern Cordillera (EC), Interandean zone (IAZ), Subandean zone (SAZ), and Chaco Plain (Figures 1 and 2). The abrupt steps in elevation and structural level between these zones are interpreted as a consequence of emplacement of thick basement thrust sheets, and the presence of large-scale footwall ramps at depth (Kley et al., 1996; McQuarrie, 2002; Müller et al., 2002).

## 2.1. Stratigraphic Framework

The stratigraphy in the central Andean fold-thrust belt consists of an ~8- to 15-km-thick package of Phanerozoic, predominantly siliciclastic sedimentary rocks (Sempere, 1995). However, stratigraphic thicknesses differ by several kilometers both along and across strike due in part to pre-Andean tectonism (McGroder et al., 2015; Starck, 1995; Tankard et al., 1995), as well as variations in accommodation space during development of the Cenozoic foreland basin (e.g., Cardozo & Jordan, 2001; Horton, 1999; Horton & DeCelles, 1997). The across-strike variability in the stratigraphic section at ~21°S is documented from field observations and a restored cross section (e.g., Anderson et al., 2017).

In southern Bolivia, the EC deforms an ~8- to 11-km-thick section of upper Cambrian to Ordovician, low-grade metasedimentary rocks (Egenhoff et al., 2002; Jacobshagen et al., 2002; Müller et al., 2002), which is overlain by >3 km of unmetamorphosed Mesozoic–Cenozoic rocks (DeCelles & Horton, 2003; Horton, 1998). Mesozoic rocks consist of a ~0.5-km-thick section of Late Cretaceous marine strata that are regionally correlative across the EC and Altiplano (Horton et al., 2001; Sempere et al., 1997; Welsink et al., 1995), and locally include >1 km of Jurassic rift-related deposits in the central EC (Sempere et al., 2002). Cenozoic rocks include ~3 km of

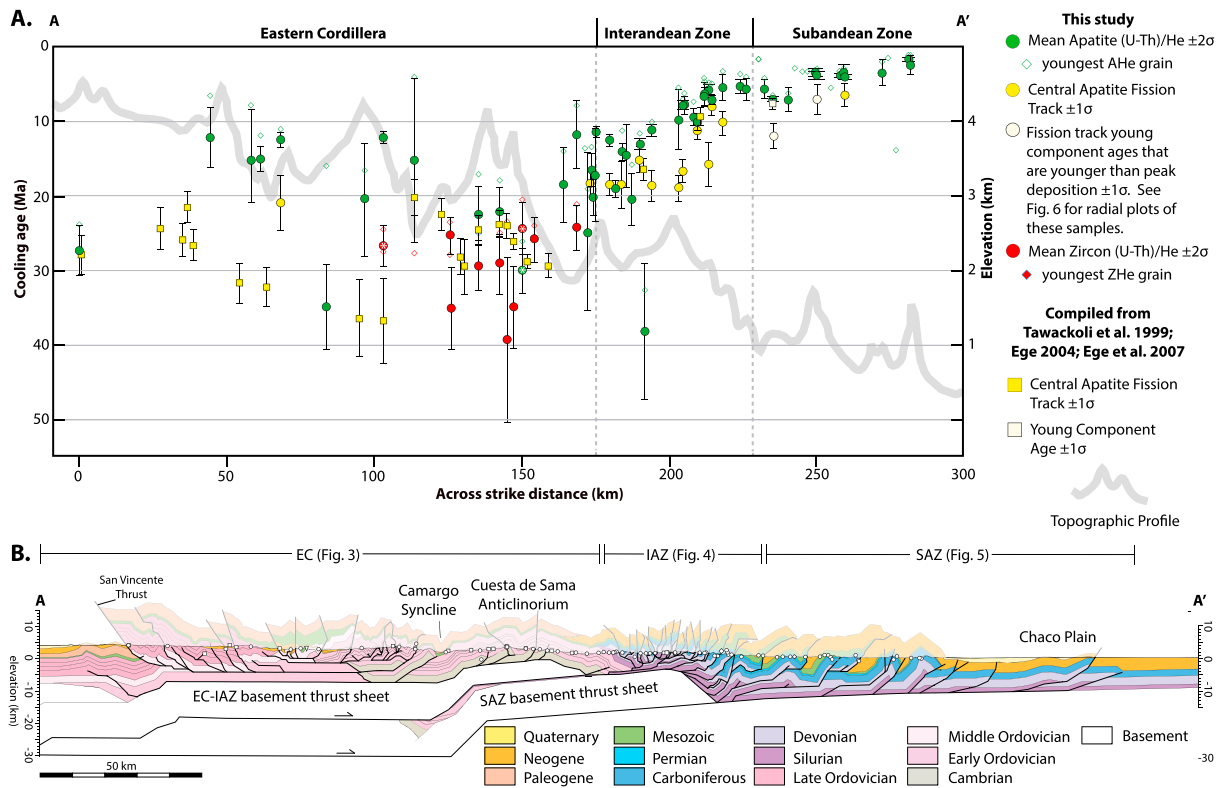


**Figure 2.** (a) Across-strike distribution of reset cooling ages in the Eastern Cordillera (EC), Interandean zone (IAZ), and Subandean zone (SAZ) between 21 and 22°S. White asterisks denote samples with inverted AHe and ZHe ages. (b) Balanced cross section through the EC, IAZ, and SAZ (simplified from Anderson et al., 2017), showing the locations of zone-specific cross sections in Figures 3–5.

Paleogene synorogenic deposits (DeCelles & Horton, 2003) and ~0.5–2.5 km of Neogene intermontane basin deposits (Horton, 1998, 2005; Müller et al., 2002).

At the EC-IAZ boundary, the Paleozoic section transitions eastward from an ~8-km-thick section of Cambrian-Ordovician rocks in the eastern EC to a ~4.5-km-thick section of Silurian-Permian rocks in the IAZ (Anderson et al., 2017; Kley, 1996). Gravimetric modeling and crustal velocity data suggest that Silurian rocks in the IAZ and SAZ likely overlie crystalline basement rather than the thick package of Ordovician-Cambrian metasedimentary rocks observed in the EC (Kley et al., 1996; Schmitz & Kley, 1997). Mesozoic-Cenozoic rocks are not preserved in the IAZ (Figure 1). However, Neogene apatite fission track (AFT) ages and thermal modeling indicate that at least ~3 km of Mesozoic-Cenozoic rocks were deposited in the IAZ but were subsequently eroded (Ege et al., 2007).

The Silurian-Permian section thickens eastward from ~4.5–5 km in the eastern IAZ to ~6–6.5 km in the SAZ and Chaco Plain (Anderson et al., 2017; Baby et al., 1992; Dunn et al., 1995; Uba et al., 2009). Conversely, Mesozoic rocks thin eastward from 1.2–1.8 km in the western SAZ (Anderson et al., 2017) to <0.2 km in the eastern SAZ and Chaco Plain (Dunn et al., 1995; Uba et al., 2009). In the SAZ and Chaco plain, >4 km of Oligocene-Quaternary, synorogenic sedimentary rocks disconformably overlie Jurassic-Cretaceous rocks (Calle et al., 2018; Uba et al., 2005, 2009).

## 2.2. Thrust Belt Structure, Shortening, and Kinematic Development at ~21°S

The Altiplano is bound on the west by the volcanic arc (the Western Cordillera) and on the east by the EC (Figure 1b). At ~21°S, the western part of the Altiplano is characterized by two doubly vergent thrust systems, and the eastern part is an E-vergent thrust system linked to the EC (Elger et al., 2005).

In southern Bolivia, the EC is divided into a western backthrust zone and an eastern forethrust zone (Anderson et al., 2017; Müller et al., 2002), centered about an axis along a proposed Mesozoic rift system



(Sempere et al., 2002; Figure 2). The EC is structurally elevated ~6 km relative to the adjacent Altiplano and IAZ (Anderson et al., 2017) and is bound on the west by the W-vergent San Vicente thrust and on the east by the Cuesta de Sama anticlinorium (Figure 2; Kley, 1996; Kley et al., 1997; Müller et al., 2002). Thrust faults in the EC detach the thick Cambrian-Ordovician section above a ~10 km deep, subhorizontal décollement located at the basement-cover interface (e.g., Allmendinger & Zapata, 2000; Anderson et al., 2017; Schmitz & Kley, 1997; Wigger et al., 1994).

At the EC-IAZ boundary, the basal décollement cuts upward from Cambrian-Ordovician rocks at the basement-cover interface to a regional décollement within Silurian shale, which persists below both the IAZ and SAZ (Baby et al., 1992; Dunn et al., 1995). The IAZ consists of a western backthrust system and an eastern forethrust system (Figure 2; Anderson et al., 2017). Thrust faults are closely spaced, with 2- to 4-km-thick thrust sheets exposing mainly Silurian-Devonian rocks (Anderson et al., 2017; Kley, 1996).

The SAZ consists of four major E-vergent thrust sheets defined by 10- to 20-km wavelength, 4- to 6-km-amplitude, fault-bend folds deformed above a 10- to 12-km-deep décollement in Silurian rocks, with secondary detachment levels in Devonian and Triassic rocks (Baby et al., 1992; Dunn et al., 1995).

The Chaco Plain is the locus of active deformation and modern foreland basin sedimentation (Brooks et al., 2011; Horton & DeCelles, 1997). Gentle folds (5–15° limb dips) and low-offset (~1–5 km) thrust faults are concealed beneath Quaternary sedimentary cover between the topographic front of the mountain belt and the active, emergent thrust front ~60 km to the east (Baby et al., 1992; Brooks et al., 2011; Dunn et al., 1995; Horton & DeCelles, 1997; Uba et al., 2009).

Much of the kinematic development of the fold-thrust belt in the central Andes has been tied to the east vergent stacking of two ~10- to 15-km-thick basement thrust sheets (e.g., Anderson et al., 2017; Eichelberger et al., 2013; Horton, 2005; McQuarrie, 2002; McQuarrie et al., 2005; McQuarrie, Barnes, & Ehlers, 2008; Rak et al., 2017). Shortening of the sedimentary cover in the EC, IAZ, and eastern Altiplano at ~21°S is linked to emplacement of the upper basement thrust sheet, whereas deformation in the SAZ is linked to motion on the lower sheet (Figure 2) (Anderson et al., 2017). In the EC and eastern Altiplano, the upper basement sheet was wedged eastward along a floor thrust as slip was fed into overlying sedimentary cover by a W-vergent roof thrust system located at the basement-cover interface (Anderson et al., 2017; Horton, 2005). Conversely, the sedimentary cover in the IAZ was imbricated in front of the eastward advancing upper basement thrust sheet (Anderson et al., 2017). Similarly, the sedimentary cover in the SAZ was deformed in front of the lower basement thrust sheet, as the rocks in the EC and IAZ were passively translated eastward (Anderson et al., 2017; Kley, 1996). The SAZ-IAZ boundary throughout the central Andes is kinematically defined at the surface as the easternmost thrust sheet in the sedimentary cover sequence that the upper basement thrust sheet feeds slip into (Anderson et al., 2017; Eichelberger et al., 2013; McQuarrie, 2002; McQuarrie, Barnes, & Ehlers, 2008). In the western Altiplano, slip was fed into the sedimentary cover via distributed basement deformation or by a basement thrust sheet with a footwall ramp located below the Western Cordillera (Elger et al., 2005).

A balanced cross section estimate of total shortening for the retroarc fold-thrust belt at ~21°S is  $337 \pm 69$  km ( $36 \pm 7\%$ ), which accounts for 90–118% of the crustal area observed today (Anderson et al., 2017). The Altiplano accounts for only ~65 km (23%) of the total strain (Elger et al., 2005), with the majority of shortening accommodated in the EC (120 km), IAZ (70 km), and SAZ (82 km; Anderson et al., 2017). Total shortening at this latitude is similar to published estimates between ~18 and 20° S (Eichelberger et al., 2013; McQuarrie, 2002), which suggests a general consistency in kinematic development of the thrust belt between 18°S and 21°S (Arriagada et al., 2008; Eichelberger & McQuarrie, 2015).

### 2.3. Published Deformation Timing Constraints

AFT ages record the initiation of exhumation-related cooling and inferred contractional deformation between ~36 and 40 Ma in the central EC at 21.5°S (Ege et al., 2007). Westward and eastward expansion of deformation from the central EC occurred between ~33 and 27 Ma, reaching the EC-Altiplano boundary by ~27 Ma and the EC-IAZ boundary by ~30 Ma (Ege et al., 2007; Müller et al., 2002). The transition from rapid sediment accumulation in a foredeep depositional environment to slow sediment accumulation in an intermontane setting at ~25 Ma marks diminished deformation in the EC (Horton, 2005). Oligocene to Miocene intermontane basins in the central and western EC record localized sedimentation and low magnitude

out-of-sequence deformation that began by ~26 Ma (Horton, 2005) but was completed prior to the ~12- to 10-Ma development of the San Juan del Oro erosional surface (Gubbels et al., 1993; Hérail et al., 1996; Horton, 1998; Kennan et al., 1997; Müller et al., 2002). In the Altiplano, Cenozoic sediments and AFT cooling ages record deformation at ~30–27 and ~19–8 Ma (Ege et al., 2007; Elger et al., 2005).

The onset of shortening in the IAZ can only be broadly inferred from the ~25-Ma shift in sedimentation rates that marks the migration of deformation out of the EC (Horton, 2005), and a single ~18 Ma AFT age in the western IAZ (Ege et al., 2007). Maximum depositional ages of Neogene growth strata indicate that deformation arrived in the eastern IAZ no earlier than ~20 Ma (Calle et al., 2018).

In southern Bolivia, the rapid increase in accumulation rates of synorogenic sediment between ~12.5 and ~10.5 Ma is inferred as the timing of initial deformation in the western SAZ (Uba et al., 2007, 2009). This is consistent with new cooling ages at 20°S that suggest an  $11 \pm 3$ -Ma onset of deformation in the SAZ (Lease et al., 2016). In the eastern SAZ, growth relationships define active shortening in the frontal-most anticline at ~2.1 Ma (Hulka, 2005; Uba et al., 2009). The majority of shortening in the Chaco Plain occurred after 2.1 Ma (Brooks et al., 2011; Costa et al., 2006; Uba et al., 2009).

### 3. Methods

Exhumation-related cooling in contractional mountain belts is the result of thrust-induced rock uplift acting in concert with erosion (e.g., Willett & Brandon, 2002). Therefore, cooling ages in fold-thrust belts are commonly interpreted to record the vertical erosional component of transport toward the surface, and to track the onset of deformation (e.g., Barnes et al., 2006, 2008; McQuarrie, Barnes, & Ehlers, 2008; Reiners & Brandon, 2006; Willett, 1999; Willett & Brandon, 2002). In the central Andes, total Cenozoic exhumation is on the order of 8–10 km or less (Barnes et al., 2008; Reiners et al., 2015), and regional Cenozoic cooling is limited to temperatures below 240 °C (Barnes et al., 2008). Therefore, we utilize apatite (U-Th)/He (AHe), AFT, zircon (U-Th)/He (ZHe), and zircon fission track (ZFT) thermochronometry as they provide details on the timing and rates of cooling over a temperature range of ~40–240 °C and crustal depths of ~2–12 km (Reiners et al., 2005).

Paleozoic-Mesozoic sedimentary units were sampled along an E-W transect between 20°45'S and 21°45'S, which spans from the modern deformation front to the Altiplano (Figures 1 and supporting information S1–S3). Here we present 59 new AHe ages, 20 new ZHe ages, 19 new AFT ages, and 2 new ZFT ages from 67 samples, along with 22 published AFT ages (Ege, 2004; Ege et al., 2007; Tawackoli et al., 1996; Tables 1–3). All samples are placed within a detailed structural context, as determined from geologic mapping and a balanced cross section constructed through the thrust belt at this latitude (Anderson et al., 2017).

#### 3.1. (U-Th)/He Thermochronometry

In apatite and zircon, helium retention is sensitive over a range of temperatures known as the helium partial retention zone (PRZ; Farley, 2002; Wolf et al., 1998). For apatite the helium PRZ is located between temperatures of 40–80 °C (Farley, 2002), and for zircon the helium PRZ is between temperatures of ~130–200 °C (Wolfe & Stockli, 2010). However, for typical orogenic cooling rates (~10 °C/Myr) and grain sizes between ~65 and 100  $\mu\text{m}$  (e.g., Reiners et al., 2005), the simplified concept of closure temperature can be applied (Dodson, 1973). The closure temperature ranges for the AHe and ZHe systems are  $\sim 65 \pm 5$  °C (Farley, 2000; Flowers et al., 2009; Shuster et al., 2006) and  $\sim 180 \pm 10$  °C (Guenther et al., 2013; Reiners et al., 2004; Wolfe & Stockli, 2010), respectively. Analytical procedures, supporting data, and individual grain ages for (U-Th)/He analyses are reported in the SI, and mean sample ages are reported in Tables 1–3.

#### 3.2. Fission Track Thermochronometry

Fission tracks within apatite and zircon are partially retained over a range of temperatures referred to as the partial annealing zone (PAZ; Gleadow et al., 1986). The AFT PAZ is between temperatures of ~60–120 °C, and the AFT system has a nominal closure temperature of  $\sim 110 \pm 10$  °C at orogenic cooling rates (Gleadow et al., 1986; Gleadow & Duddy, 1981; Green et al., 1986; Ketcham et al., 2007). However, apatite with higher Cl content or etch pit diameter (Dpar) are more resistant to annealing and have a higher closure temperature (Donelick et al., 2005). Though such compositions are relatively rare, variable annealing of individual grains may explain some mixed ages (Armstrong, 2005). Laboratory experiments indicate that the ZFT PAZ is between temperatures of ~262–330 °C (Yamada et al., 2007), but field-based estimates of the ZFT nominal

**Table 1**  
Summary of Eastern Cordillera Apatite (U-Th)/He, Apatite Track, and Zircon (U-Th)/He Data

Sample	Formation	Coordinates		Mean AHe Age (Ma)	Error (2 $\sigma$ )	n (a.m)	AFT central age (Ma)	Error (1 $\sigma$ )	N <sub>a</sub>	P ( $\chi^2$ ) %	Mean ZHe age (ma)	Error (2 $\sigma$ )	n (a.m)	ZFT central age (Ma)	Error (1 $\sigma$ )	N <sub>a</sub>	P ( $\chi^2$ ) %
		Longitude	Latitude														
ECO293, EC64 <sup>a</sup>	O. Marquina Fm.	-66.2837	-21.3535	27.3	3.2	(6.4)	27.7	2.5	30	54	179.5 <sup>P</sup>	112.6	(6.6)	—	—	—	—
ECO270	O. Marquina Fm.	-66.1494	-21.4192	106.1	22.2	(6.6)	—	—	—	—	—	—	—	—	—	—	—
ECO6 <sup>a</sup>	O. Marquina Fm.	-66.0291	-21.1022	—	—	—	24.3	2.8	15	80	—	—	—	—	—	—	—
ECO8 <sup>a</sup>	O. Kolipani Fm.	-65.9757	-21.1235	—	—	—	25.8	2.1	30	<5	—	—	—	—	—	—	—
ECO9 <sup>a</sup>	O. Tapial Fm.	-65.9301	-21.1641	—	—	—	21.5	2.1	30	99	—	—	—	—	—	—	—
EC73 <sup>a</sup>	O. Marquina Fm.	-65.9062	-21.4280	—	—	—	26.7	2.1	20	96	—	—	—	—	—	—	—
ECO299	O. Angosto Fm.	-65.8579	-21.4498	12.1	4.0	(6.5)	—	—	—	—	—	—	—	—	—	—	—
TU38 <sup>a</sup>	O. Jurcurma Fm.	-65.7497	-21.4068	—	—	—	31.5	2.6	20	93	—	—	—	—	—	—	—
ECO224	O. Jurcurma Fm.	-65.7223	-21.4098	15.2	6.8	(6.4)	—	—	—	—	—	—	—	—	—	—	—
ECO212	O. Jurcurma Fm.	-65.7036	-21.5082	14.9	1.8	(6.5)	—	—	—	—	—	—	—	—	—	—	—
TW	O. Protero Fm.	-65.6170	-21.5162	—	—	—	32.1	4.5	?	?	—	—	—	—	—	—	—
ECO200	O. Protero Fm.	-65.6561	-21.5084	12.4	1.0	(6.6)	20.9	3.7	9	98	—	—	—	—	—	—	—
ECO175	O. Agua y Toro Fm.	-65.5017	-21.3532	34.9	5.8	(6.4)	—	—	—	—	—	—	—	—	—	—	—
EC77 <sup>a</sup>	O. Pirancha Fm.	-65.4004	-21.4169	—	—	—	36.4	5.2	17	77	—	—	—	—	—	—	—
ECO143	O. Agua y Toro Fm.	-65.3817	-21.4186	20.3	7.6	(3.2)	—	—	—	—	—	—	—	—	—	—	—
ECO22, EC78 <sup>a</sup>	O. Cienegillas	-65.3239	-21.3978	12.1 <sup>sg</sup>	0.7	(3.1)	36.7 <sup>mr</sup>	5.7	34	<5	346.5 <sup>P</sup>	18.8	(4.3)	—	—	—	—
ECO21	O. Obispo	-65.3096	-21.3896	—	—	—	—	—	—	—	26.6	2.8	(5.4)	—	—	—	—
ECO88	O. Pirancha Fm.	-65.2227	-21.4444	15.3	11	(6.2)	—	—	—	—	262.5 <sup>P</sup>	95.4	(6.6)	—	—	—	—
ECO92, EC83 <sup>a</sup>	O. Pirancha Fm.	-65.1845	-21.2743	—	—	—	20.1	2.4	27	41	88.3 <sup>P</sup>	75.2	(6.6)	—	—	—	—
EC35 <sup>a</sup>	O. Obispo Fm.	-65.1230	-21.2898	—	—	—	22.4	2.1	22	80	—	—	—	—	—	—	—
ECO93	ε Torhuayco Fm.	-65.1661	-21.8187	—	—	—	—	—	—	—	35.1	5.4	(6.5)	136.8	7.1	20	96.2
ECO72	O. Iscayachi Fm.	-65.0883	-21.4838	—	—	—	—	—	—	—	25.2	2.6	(6.4)	—	—	—	—
EC80 <sup>a</sup>	O. Cienegillas Fm.	-65.0501	-21.3587	—	—	—	28.2	2.4	30	99	—	—	—	—	—	—	—
EC82 <sup>a</sup>	O. Cienegillas Fm.	-65.0371	-21.3584	—	—	—	29.3	3.7	31	58	—	—	—	—	—	—	—
ECO61, EC81 <sup>a</sup>	ε Sama Fm.	-65.0124	-21.5139	22.4	3.6	(6.6)	24.5	2.0	30	44	29.5	3.0	(6.4)	146.9	7.4	20	34.0
ECO35, EC30 <sup>a</sup>	O. Iscayachi Fm.	-64.9493	-21.4873	22.0	3.2	(6.4)	23.8	1.7	22	73	29.1	4.0	(6.5)	—	—	—	—
ECO02, EC29 <sup>a</sup>	ε Sama Fm.	-64.9230	-21.4855	—	—	—	23.9	1.6	35	92	39.2	11.0	(4.4)	—	—	—	—
ECO05, SA19 <sup>a</sup>	ε Sama Fm.	-64.9143	-21.4992	—	—	—	26.1	2.2	21	60	34.9	11.0	(6.6)	—	—	—	—
ECO04	O. Iscayachi Fm.	-64.8741	-21.4597	29.9	3.0	(6.6)	—	—	—	—	24.4	3.4	(6.4)	—	—	—	—
SA20 <sup>a</sup>	O. Iscayachi Fm.	-64.8491	-21.4535	—	—	—	28.8	1.9	33	70	—	—	—	—	—	—	—
ECO01	O. Iscayachi Fm.	-64.8339	-21.4727	—	—	—	—	—	—	—	25.7	3.0	(3.3)	—	—	—	—
SA21 <sup>a</sup>	O. Cienegillas Fm.	-64.7819	-21.4282	—	—	—	29.3	3.2	15	16	—	—	—	—	—	—	—
ECO53	O. Cienegillas Fm.	-64.7566	-21.3297	—	—	—	—	—	—	—	95.6 <sup>P</sup>	8.6	(6.6)	—	—	—	—
ECO56	O. Obispo Fm.	-64.7351	-21.3447	18.4	5.0	(5.4)	—	—	—	—	91.0 <sup>P</sup>	16.2	(6.5)	—	—	—	—
ECO68	O. Sella Fm.	-64.6929	-21.3950	11.8	4.4	(3.3)	—	—	—	—	24.1	3.0	(6.4)	—	—	—	—
ECO-IAZ01	O. Sella Fm.	-64.6745	-21.3891	—	—	—	—	—	—	—	86.2 <sup>P</sup>	46.8	(5.5)	—	—	—	—
ECO-IAZ02	S. Cancaniri Fm.	-64.6552	-21.3840	24.9	10.4	(5.3)	—	—	—	—	175.6 <sup>P</sup>	182.0	(5.4)	—	—	—	—
ECO-IAZ03	S. Tarabuco Fm.	-64.6420	-21.3743	15.6	2.0	(6.5)	18.2	1.5	27	99.9	187.6 <sup>P</sup>	63.8	(5.5)	—	—	—	—
ECO-IAZ04	D. Santa Rosa Fm.	-64.6371	-21.3789	20.2	2.4	(6.5)	—	—	—	—	318.1 <sup>P</sup>	41.4	(6.5)	—	—	—	—
ECO-IAZ05	D. Huamampampa Fm.	-64.6311	-21.3836	17.2	6.2	(6.6)	—	—	—	—	272.4 <sup>P</sup>	45.2	(6.5)	—	—	—	—

Note. See supporting information data file SM1 for individual (U-Th)/He aliquot data and supporting information data file SM2 for individual grain fission track age data. n (a.m): number grains analyzed, grains used in mean age; n<sub>a</sub>: number of grain ages for apatite fission track (AFT) or zircon fission track (ZFT).

<sup>a</sup>AFT age from Ege et al. (2007). <sup>b</sup>AFT age from Tawackoli (1999). <sup>P</sup>Partial reset. <sup>mr</sup>Mixed reset. <sup>sg</sup>Single grain age.

**Table 2**  
Summary of Interandean Zone Apatite (U-Th)/He and Apatite Fission Track Ages

Sample	Formation	Coordinates		Mean AHe age (Ma)	Error (2 $\sigma$ )	n (a.m.)	AFT central age (Ma)	Error (1 $\sigma$ )	N <sub>a</sub>	P ( $\chi^2$ ) %	AFT YC (Ma)	Error (1 $\sigma$ )	Mean ZHe age (Ma)	Error (2 $\sigma$ )	n
		Longitude (°S)	Latitude (°W)												
IAZ50	D. Ida Fm.	-64.6285	-21.3853	11.4 <sup>sg</sup>	0.7	(3,1)	—	—	—	—	—	—	—	—	—
IAZ51	S. Tarabuco Fm.	-64.6289	-21.5624	12.5 <sup>sg</sup>	0.8	(6,1)	18.5	1.5	40	>99.9	—	—	—	—	—
IAZ52	D. Huamampampa Fm.	-64.5693	-21.3818	19.0 <sup>sg</sup>	1.1	(3,1)	—	—	—	—	—	—	—	—	—
IAZ06	D. Santa Rosa Fm.	-64.5479	-21.4135	14.1	2.4	(6,4)	18.5	3.1	20	99.4	—	—	—	—	—
IAZ53	P. Cangapi Fm.	-64.5335	-21.4050	14.5	4.2	(6,5)	—	—	—	—	—	—	—	—	—
IAZ27	D. Ida Fm.	-64.5399	-21.5220	20.5	3.2	(4,4)	—	—	—	—	—	—	—	—	—
IAZ24	S. Tarabuco Fm.	-64.4930	-21.4521	13.1	0.8	(6,6)	15.1	1.7	27	99.8	—	—	—	—	—
EC23 <sup>a</sup>	D. Santa Rosa Fm.	-64.4877	-21.4415	—	—	—	16.4	1.4	23	64	—	—	—	—	—
IAZ23	S. Tarabuco Fm.	-64.4771	-21.4419	38.1	9.0	(6,6)	—	—	—	—	—	—	—	—	—
IAZ21	S. Tarabuco Fm.	-64.4447	-21.4272	11.1	0.8	(6,6)	18.6	1.7	20	>99.9	—	—	—	—	—
IAZ13	D. Huamampampa Fm.	-64.3603	-21.4532	9.9	4.0	(6,6)	18.8	1.7	20	>99.9	—	—	—	—	—
IAZ11	D. Ida Fm.	-64.3494	-21.4547	7.8	0.6	(5,5)	16.7	1.6	14	97.8	—	—	—	—	—
IAZ10	D. Huamampampa Fm.	-64.3435	-21.4552	7.8	1.2	(5,5)	—	—	—	—	—	—	—	—	—
IAZ403	C. Tupambi Fm.	-64.3122	-21.4769	9.4	1.2	(6,6)	—	—	—	—	—	—	—	—	—
IAZ347	D. Iquiri Fm.	-64.2977	-21.4822	10.0 <sup>sg</sup>	0.6	(6,1)	11.1	1.1	30	99.9	—	—	—	—	—
EC19 <sup>b</sup>	Permo-Triassic	-64.2841	-21.4030	—	—	—	9.2	1.2	31	44	—	—	—	—	—
IAZ54	J-K. Tapacua Fm.	-64.2777	-21.4159	6.3	1.6	(6,4)	—	—	—	—	—	—	—	—	—
IAZ55	P. Cangapi Fm.	-64.2747	-21.4291	6.6	1.2	(6,6)	—	—	—	—	—	—	—	—	—
IAZ56	C. Escarpment Fm.	-64.2612	-21.4362	5.9	0.8	(6,6)	15.8	2.9	14	98.1	—	374.9 <sup>u</sup>	14.4	(10,10)	—
IAZ344	C. Tupambi Fm.	-64.2630	-21.4935	7.1	1.2	(6,6)	8.0	1.2	20	97.3	—	—	—	—	—
IAZ342	C. Escarpment Fm.	-64.2374	-21.4914	5.5	1.8	(6,5)	10.1	1.6	20	99.2	—	—	—	—	—
IAZ57	J-K. Ichoa Fm.	-64.1492	-21.4706	5.3	1.0	(6,5)	—	—	—	—	—	—	—	—	—
IAZ58	T. Ipaguzo Fm.	-64.1395	-21.4640	5.6	1.6	(6,4)	79.9 <sup>pr</sup>	35.6	6	0.01	26.2	9.3	—	—	—

Note. See supporting information data file SM1 for individual (U-Th)/He aliquot data and supporting information data file SM2 for fission track single grain age data. YC: Young component; n (a.m.): number grains analyzed; grains used in mean age; n<sub>a</sub>: number of grains ages for apatite fission track (AFT) or ZFT.

<sup>a</sup>Ege et al. (2007).

<sup>b</sup>Ege (2004).

<sup>sg</sup>Single grain age or only has one AHe age younger than the AFT central age.

<sup>u</sup>Unreset.

<sup>pr</sup>Partial reset.

closure temperature are lower ( $\sim 240 \pm 10$  °C) at orogenic cooling rates of  $\sim 10$  °C/Myr (Bernet, 2009; Brandon et al., 1998).

For fission track samples, the  $\chi^2$  statistic is commonly utilized as a measure of variance of the grain age distribution in a sample (Galbraith, 1981; Green, 1981). Samples with a low age variance [ $P(\chi^2) > 5\%$ ] are classified as homogenous (i.e., confirming the null hypothesis that all grains belong to a single age population) and the sample cooling age is reported as a central age (e.g., weighted mean of the log normal distribution of single grain ages; Galbraith, 2005; Gallagher et al., 1998). For overdispersed AFT ages [ $P(\chi^2) < 5\%$ ], we employed radial plots (Galbraith, 2005) using RadialPlotter software (Vermeesch, 2009) to resolve different age populations present in the sample, which can be used to define a young, reset component (e.g., Lease et al., 2016) and to provide context for the position of the sample relative to the PAZ (e.g., Armstrong, 2005; O'Sullivan & Parrish, 1995). An age distribution on a radial plot that is characterized by predominantly young grains with only a minor population of older grains more resistant to annealing is characteristic of a stratigraphic position near the base of the PAZ and will most closely approximate the onset of rapid cooling in the absence of a fully reset and homogenous age (O'Sullivan & Parrish, 1995). However, the young component age for samples that were located within the middle and upper part of the AFT PAZ only provides a maximum time constraint for the onset of cooling (O'Sullivan & Parrish, 1995). Fission track ages and  $\chi^2$  values are shown in Tables 1–3, and individual grain data are reported in the supporting information (Table S2).

### 3.3. Sample Classification

We classified cooling ages as reset, mixed reset, partially reset, or unreset by post-depositional burial and reheating (e.g., Barnes et al., 2006; Enkelmann et al., 2015; Lease et al., 2016). Reset samples consist of a single age component younger than the depositional age, mixed reset samples contain multiple age components that are younger than deposition, partially reset samples exhibit age components that are both younger and older than deposition, and unreset samples are defined by age components that predate deposition (Barnes et al., 2006). Reset samples that yielded a Cenozoic cooling age are interpreted to record erosionally driven exhumation during Andean orogenesis (e.g., McQuarrie, Barnes, & Ehlers, 2008). In the central Andes, reset samples with the oldest Cenozoic cooling ages are



**Table 3**  
Summary of Subandean Zone Apatite (U-Th)/He and Apatite Fission Track Data

Sample	Formation	Coordinates		AHe mean age (Ma)	Error (2 $\sigma$ )	<i>n</i> (a,m)	AFT central age (Ma)	Error (1 $\sigma$ )	<i>N<sub>a</sub></i>	<i>P</i> ( $\chi^2$ )%	AFT young comp. (Ma)	Error (1 $\sigma$ )
		Longitude (°S)	Latitude (°W)									
SAZ63	Cz. Petaca Fm.	−64.1006	−21.4477	90.8 <sup>pr</sup>	45.6	(6,6)	—	—	—	—	—	—
SAZ62	Ṭ Ipaguazu Fm.	−64.0818	−21.4460	5.6	1.2	(6,5)	37.7 <sup>mr</sup>	11.9	20	0	13.7	4.4
SAZ61	C. San Telmo Fm.	−64.0603	−21.4449	7.0	0.2	(6,2)	29.4 <sup>mr</sup>	10.4	20	<0.01	12.3	1.7
BE26 <sup>a</sup>	upper Carboniferous	−64.0520	−21.3963	—	—	—	28.6 <sup>mr</sup>	9.8	30	<5	7.37	0.67
SAZ60	Ṭ Ipaguazu Fm.	−63.9981	−21.4210	7.1	1.6	(6,4)	—	—	—	—	—	—
SAZ54	Cz. Petaca Fm.	−63.7635	−21.0486	41.4 <sup>pr</sup>	30.5	(6,4)	—	—	—	—	—	—
SAZ53	K. Castellon Fm.	−63.7651	−21.0611	35.1 <sup>mr</sup>	16.5	(6,6)	—	—	—	—	—	—
SAZ52	K. Tapehua Fm.	−63.7565	−21.0678	67.9 <sup>mr</sup>	34.4	(4,4)	—	—	—	—	—	—
SAZ51	P. Viteacua Fm.	−63.7526	−21.0714	3.4	0.6	(6,4)	—	—	—	—	—	—
SAZ50	C. Escarpment Fm.	−63.7490	−21.0737	3.8	0.6	(6,6)	37.9 <sup>mr</sup>	10.8	15	0	7.2	2.0
SAZ43	Cz. Petaca Fm.	−63.7297	−21.2196	174.5 <sup>pr</sup>	144.5	(6,4)	—	—	—	—	—	—
SAZ42	C. Escarpment Fm.	−63.7041	−21.1847	3.8	0.4	(6,4)	—	—	—	—	—	—
SAZ41	C. Tupambi Fm.	−63.6982	−21.1799	3.6	1.0	(6,5)	—	—	—	—	—	—
SAZ40	D. Iquiri Fm.	−63.6960	−21.1796	4.0	0.6	(4,4)	6.3	1.5	13	98	—	—
SAZ06	C. Tarija Fm.	−63.7734	−21.6071	3.5	1.8	(6,3)	136.7 <sup>pr</sup>	26.3	20	<0.01	10.7	2.2
SAZ09	P. Vitiacua Fm.	−63.7616	−21.6368	110.5 <sup>mr</sup>	51.8	(6,6)	—	—	—	—	—	—
SAZ21	K. Ichoa	−63.4200	−20.7878	55.3 <sup>mr</sup>	22.2	(6,6)	—	—	—	—	—	—
SAZ13	C. Tarija Fm.	−63.6961	−21.8789	1.6	0.4	(6,5)	—	—	—	—	—	—
SAZ15	D. Iquiri Fm.	−63.4025	−20.7972	2.4	1.4	(6,4)	22.3 <sup>mr</sup>	6.4	11	<0.01	15.2	2.9

Note. See supporting information data file SM1 for individual (U-Th)/He aliquot data and supporting information data file SM2 for fission track single grain age data. *n* (a,m): number grains analyzed, grains used in mean age; *n<sub>a</sub>*: number of grain ages for AFT or ZFT.

<sup>a</sup>Ege (2004). <sup>pr</sup>Partial reset. <sup>mr</sup>Mixed reset.

commonly interpreted to reflect the onset of thrust-related deformation (e.g., Barnes et al., 2006, 2008, 2012; Carrapa & DeCelles, 2015; Ege et al., 2007; Eichelberger et al., 2013; Gillis et al., 2006; Lease et al., 2016; McQuarrie, Barnes, & Ehlers, 2008). However, erosional exhumation can continue after active deformation (e.g., Barnes et al., 2008; McQuarrie, Barnes, & Ehlers, 2008), may represent exhumational steady state (Willett & Brandon, 2002), or erosion may be decoupled from tectonic activity altogether (e.g., Lease & Ehlers, 2013). Therefore, we employ age-depth analysis (e.g., Stockli, 2005) and thermal modeling (e.g., Ehlers, 2005; Ketcham, 2005) in order to interpret our cooling ages and to better understand the processes that drove exhumation and cooling.

## 4. Results

### 4.1. Ages in the EC

In the EC, we report 42 new cooling ages from 28 samples of Cambrian-Devonian sedimentary rocks (Table 1 and Figure 3), which are supplemented by 17 published AFT ages (Ege et al., 2007; Tawackoli, 1999). Two samples from the stratigraphically deepest Cambrian rocks along the transect (ECO93, ECO61), located within the core of the Cuesta de Sama anticlinorium (Figure 3), yielded Cretaceous (136.8 ± 7.1 Ma) and Jurassic (146.9 ± 7.4 Ma) ZFT ages. Although both samples are homogenous and reset (Table 1), relatively low counts per individual grain (Table S2) often mean the  $\chi^2$  test may not be reliable, such that it may pass at the 5% level, but the high single grain age uncertainties can hide a true age mixing or partial resetting (Galbraith, 2005). Nevertheless, any subsequent reheating or maximum burial event that resulted in reset or partial reset ZFT ages can be no younger than the youngest ZFT individual grain age (~92.1 ± 20.6 Ma, Table S2). Given the lack of any Cenozoic individual grain ages from these samples (Table S2), burial temperatures for rocks at the deepest exposed levels of the EC likely did not exceed ZFT PAZ conditions (~230–250 °C) after the Late Cretaceous.

Mean ZHe ages in the EC vary from reset to mixed reset, and range from ~346.5 to ~24.1 Ma (Table 1 and Figure 3). Samples were collected primarily from Cambrian to Devonian rocks in the Cuesta de Sama anticlinorium, though three samples of Ordovician rocks were collected west of the Camargo syncline (Figure 3).

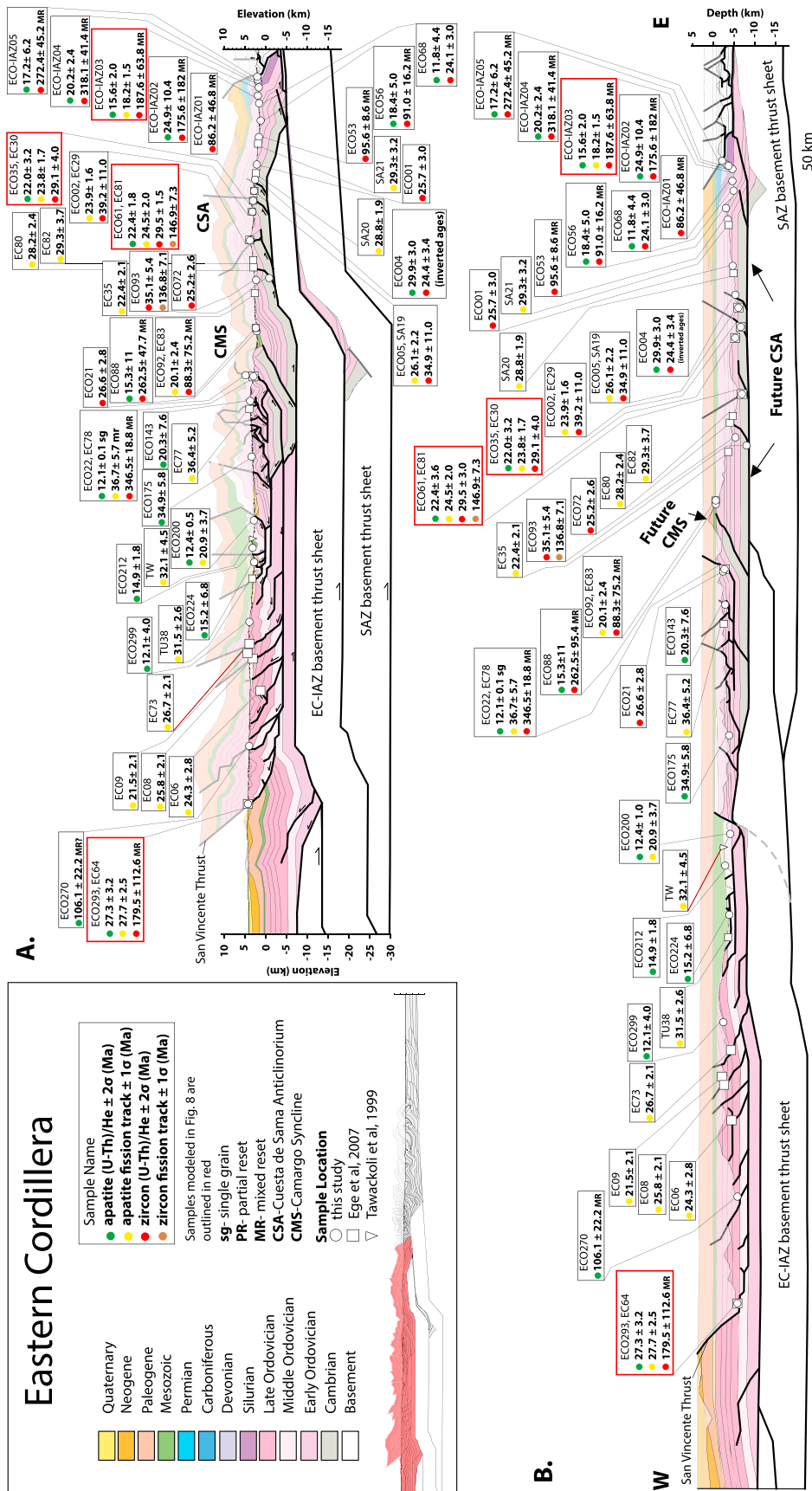


**Figure 3.** Cooling ages from the Eastern Cordillera (EC) projected onto deformed (a) and restored (b) cross sections simplified from Anderson et al. (2017). SG = single grain age; P = partial reset age; mr = mixed reset age. Samples modeled in Figure 8 are outlined in red.

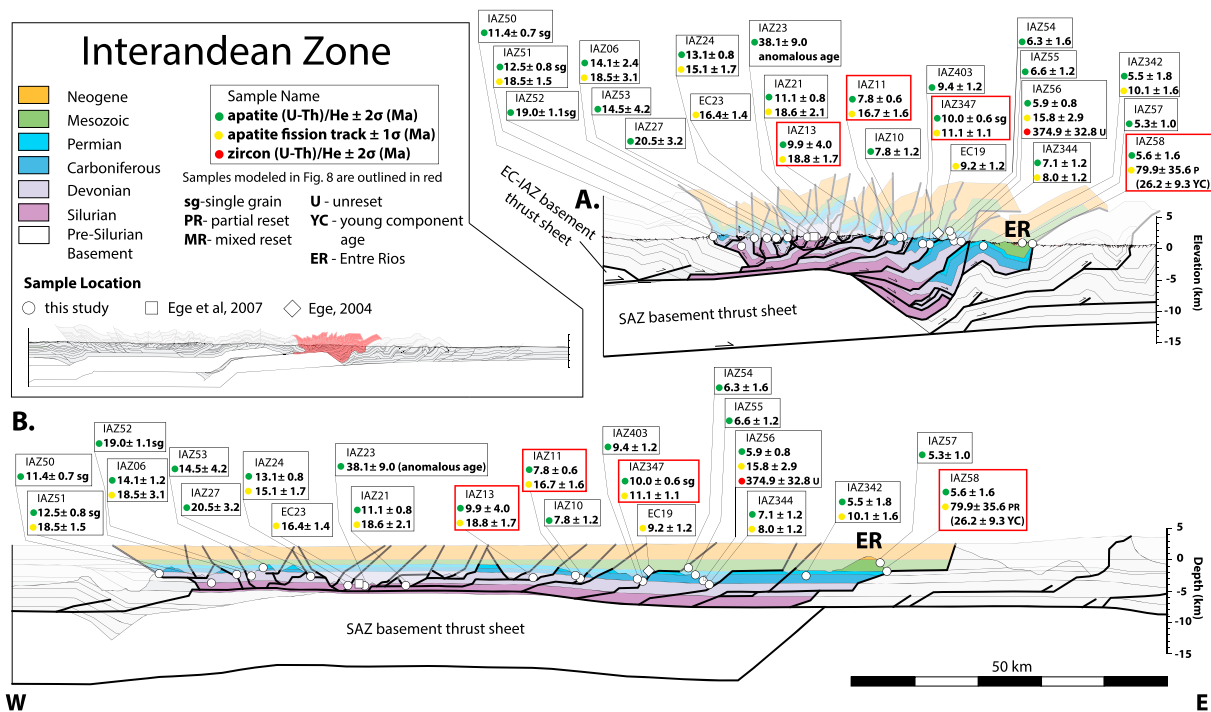


**Figure 4.** Cooling ages from the Interandean zone (IAZ) projected onto deformed (a) and restored (b) cross sections simplified from Anderson et al. (2017). SG = single grain age; U = unreset age; P = partial reset age; mr = mixed reset age; YC = young component age; ER = Entre Rios. Samples modeled in Figure 8 are outlined in red.

Mean reset ZHe ages ( $n = 9$ ) range between 39.2 and 24.1 Ma but are limited to the core of the Cuesta de Sama anticlinorium. Three of the deepest samples returned mean reset ZHe ages between 39.2 and 34.9 Ma; given that homogenous Mesozoic ZFT ages were obtained here, rocks from these depths did not exceed  $\sim 230$ – $250$  °C after the Cretaceous but were above ZHe closure ( $\sim 170$ – $190$  °C) prior to Cenozoic exhumation. Thus, the Eocene ZHe ages presumably record the onset of Andean deformation in the eastern EC. Samples collected at shallower stratigraphic depths ( $< 4$  km below the Late Cretaceous unconformity) in the eastern EC yielded mean mixed reset and unreset ZHe ages between  $\sim 346$  and  $\sim 86$  Ma.

West of the Camargo syncline, Ordovician samples from depths between  $\sim 2$  and 5 km below the Late Cretaceous unconformity yielded mean ZHe ages between  $\sim 347$  and  $\sim 180$  Ma (Table 1 and Figure 3). A third sample (ECO21) yielded a mean reset ZHe age of  $26.6 \pm 2.8$  Ma but is suspect because it restores to a shallower stratigraphic position than mixed and unreset ZHe ages from proximal samples (see SI for further discussion). Thus, maximum Cenozoic burial temperatures in the western EC likely did not exceed  $\sim 130$ – $170$  °C, even at depths of  $\sim 5$  km below the Late Cretaceous unconformity.

In zircon with very high doses of sustained radiation damage, helium retention starts to decrease, lowering the closure temperature in zircon (Guenther et al., 2013). Of the 13 mixed reset ZHe samples across the EC, nine samples display negative age-eU correlations (Table S1), a proxy for radiation damage (e.g., Guenther et al., 2013). However, the youngest individual grains in all but one of these samples (ECO22) are greater than 68 Ma, indicating that these shallow samples did not experience elevated temperatures capable of fully resetting even radiation-damaged zircons after the Mesozoic.

AFT ages across the EC (2 new, 17 published) range from  $\sim 36.7$  to  $\sim 18.2$  Ma (Table 1 and Figure 3; Tawackoli, 1999; Ege et al., 2007). Nearly all AFT ages are reset and have a single age population, which indicates that all Paleozoic rocks were at burial temperatures above  $\sim 100$ – $120$  °C prior to Cenozoic exhumation. Given the mixed and unreset ZHe ages west of the Camargo syncline, the AFT ages give the best estimate for the minimum onset of cooling in the western EC. The oldest AFT ages (31.5–36.7 Ma) are located between the Camargo syncline and the town of Tupiza. West of Tupiza, AFT ages range from 27.7 to 21.5 Ma.

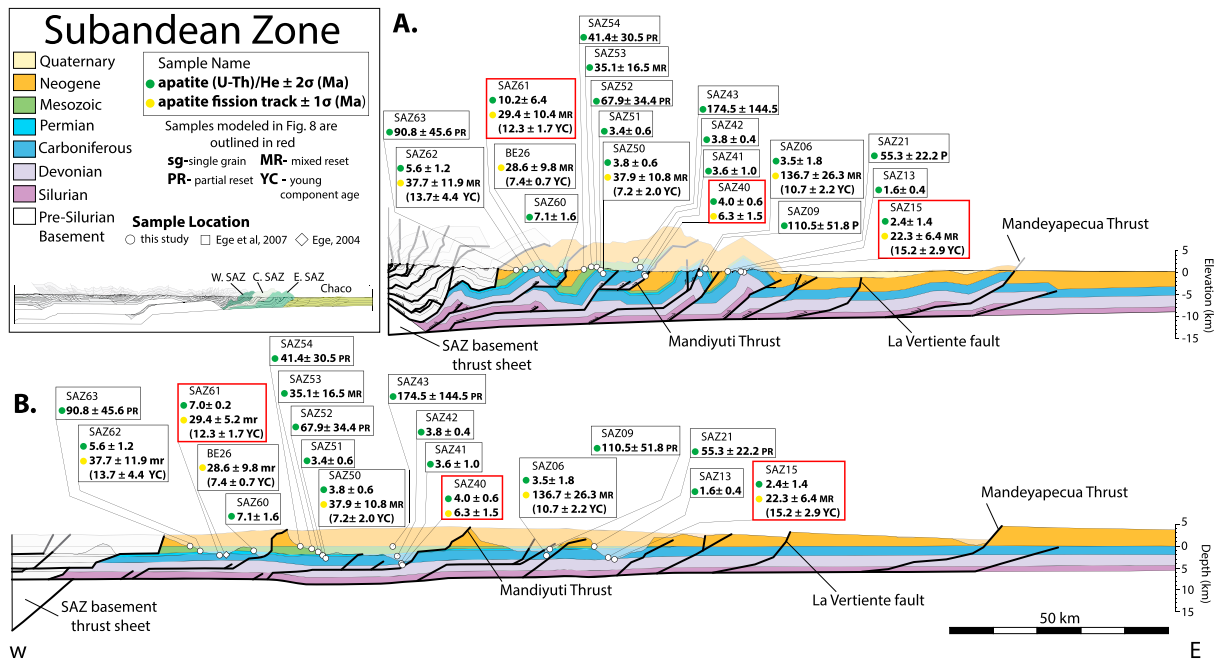


**Figure 5.** Cooling ages from the Subandean zone (SAZ) projected onto deformed (a) and restored (b) cross sections simplified from Anderson et al. (2017). SG = single grain age; P = partial reset age; mr = mixed reset age; YC = young component age. Samples modeled in Figure 8 are outlined in red.

Samples in the EC yielded mean reset AHe ages ( $n = 18$ ) between  $\sim 34.9$  and  $11.8$  Ma (Table 1 and Figure 3). Samples with multipart cooling histories (ECO61/EC81 and ECO35/EC30) show that rocks within the central part of the Cuesta de Sama anticlinorium cooled relatively rapidly from  $\sim 180$  to  $\sim 65^\circ\text{C}$  between  $\sim 30$  and  $22$  Ma, while samples along the eastern flank of the anticlinorium generally record younger cooling ages ( $\sim 25$ – $12$  Ma). West of the Camargo syncline, nearly all mean AHe ages are between  $\sim 20$  and  $12$  Ma, except at the EC-Altiplano boundary. AHe and AFT ages from a sample in the hanging wall of the San Vicente thrust (ECO293/EC64) define rapid cooling from  $\sim 110$  to  $\sim 65^\circ\text{C}$  between  $\sim 28$  and  $27$  Ma.

#### 4.2. Ages in the IAZ

In the IAZ, 33 new cooling ages were obtained from 21 samples of Silurian-Cretaceous sedimentary rocks (Table 2 and Figure 4), along with two published AFT ages (Ege, 2004; Ege et al., 2007). A single mean ZHe age of  $374.9 \pm 14.4$  Ma obtained from a Carboniferous sample in the central IAZ (IAZ56) indicates that postdepositional burial temperatures were less than  $\sim 170$ – $190^\circ\text{C}$ . All AFT samples but one (IAZ58) are homogenous and reset (Table 2), indicating postdepositional burial temperatures greater than  $\sim 110 \pm 10^\circ\text{C}$  for samples at stratigraphic levels below the Triassic, followed by widespread cooling between  $\sim 19$  and  $8$  Ma (Figure 4). The AFT ages generally become younger eastward across the IAZ but can be divided into two distinct age groups (Figure 2). AFT ages within the western IAZ range between  $\sim 19$  and  $15$  Ma ( $n = 8$ ), and between  $\sim 11$  and  $8$  Ma ( $n = 4$ ) in the eastern IAZ (excluding the partially reset sample IAZ58).

Reset mean AHe ages in the IAZ ( $n = 21$ ) range from  $\sim 38$  to  $5$  Ma (Table 2 and Figure 4). The AHe data are from samples that span from the Silurian to the Mesozoic section. The shallowest Mesozoic samples (IAZ58, IAZ57, and IAZ54) yielded fully reset mean ages between  $\sim 6.3$  and  $5.3$  Ma, indicating that Neogene burial was sufficient to reset rocks that were at the surface prior to deposition of synorogenic strata (Figure 4). The 10 samples in the IAZ with paired AHe-AFT ages show that the samples cooled through  $\sim 110^\circ\text{C}$  between  $\sim 19$  and  $8$  Ma, and through  $\sim 65^\circ\text{C}$  between  $14$  and  $5.5$  Ma. However, three samples (IAZ23, IAZ27, and IAZ52) yielded mean AHe ages ( $38.1$ ,  $20.5$ ,  $19.0$  Ma, respectively) that are older than any of the other observed AHe ages and are older than any AFT age ( $\sim 19$ – $15$  Ma range) in the western IAZ. We assume that these anomalously old AHe ages are likely due to erroneous  $\alpha$ -ejection correction resulting from uncharacterized zoning of parent nuclide or excess helium from fluid or mineral inclusions (see SI for additional discussion). Excluding these



old AHe ages, mean AHe ages from samples in the western IAZ vary between ~14.5 and ~7.8 Ma ( $n = 9$ ), and between ~10.0 and ~5.3 Ma ( $n = 9$ ) in the eastern IAZ (Figures 2 and 4).

#### 4.3. Ages in the SAZ

In the SAZ, we report 24 new cooling ages from 18 samples, accompanied by one published AFT age (Ege, 2004; Table 3). Samples were collected from Devonian to Oligocene rocks (Figure 5), which were buried beneath ~2–4.5 km of synorogenic rocks. AFT ages ( $n = 7$ ) range from ~6 to ~137 Ma. All AFT ages are overdispersed with mixed reset ages that are significantly younger than their depositional age, except sample SAZ40, which yielded a reset age of  $6.3 \pm 1.5$  Ma. This sample was collected from the stratigraphically deepest level (~8.3 km of total burial) exposed in the central SAZ. All of the other mixed reset AFT ages indicate PAZ thermal conditions for samples that restore to stratigraphic depths between ~3.5 and 6.5 km. However, using age distributions on radial plots (Figure 6), the young age components from these samples can still provide an estimate for timing of onset of exhumation across the SAZ.

AFT youngest component ages resolved from radial plots for SAZ samples range between 7.37 and 15.2 Ma (Table 3 and Figure 6). Samples BE26 and SAZ61 (Figure 6c), the two deepest samples in the western SAZ, display a well-defined population of predominantly young grains. The remaining samples have radial plot distributions showing a broad mixture of young and old grains (SAZ50, SAZ62, and SAZ15), characteristic of the middle part of the PAZ (Figure 6b), and a distinct population of older grains (SAZ06) characteristic of the upper portion of the PAZ (Figure 6a). Onset of AFT cooling in the western SAZ can be no older than the  $13.7 \pm 4.4$  Ma young component age from the sample SAZ62. Thus, the best estimate for the onset of AFT cooling in the western SAZ is between ~7 and ~12 Ma, as defined by the young component ages of BE26 ( $7.37 \pm 0.67$  Ma) and SAZ61 ( $12.3 \pm 1.7$  Ma). The onset of rapid cooling in the central SAZ is constrained by the  $6.3 \pm 1.5$  Ma reset AFT age from sample SAZ40, which overlaps within error with the  $9.6 \pm 1.9$  Ma young component age of the stratigraphically shallower sample SAZ50. In the eastern SAZ, the AFT young component ages place a maximum constraint on the onset of exhumation ( $10.7 \pm 2.2$  to  $15.2 \pm 2.9$  Ma), given that these samples were likely within the middle to upper part of the PAZ. However, middle Miocene exhumation in this part of the thrust belt is unlikely given that synorogenic sedimentary burial was active in the eastern SAZ from ~12.4 Ma until at least ~3.5 Ma, and there are no documented sedimentary growth strata in Cenozoic rocks in the anticlinal ranges of the central SAZ at this latitude (Calle, 2013; Uba et al., 2007).

Mean AHe ages in the SAZ ( $n = 18$ ) vary from 1.6 to 175 Ma (Table 3 and Figure 5). Dispersion of AHe ages greater than analytical uncertainty is common and typically results in anomalously old ages (Flowers et al., 2009; Murray et al., 2014). For samples in the SAZ where exhumational cooling is most recent, mean AHe ages calculated using apatite grains with radiation damage or excess helium due to uncharacterized inclusions, zonation, or grain boundary phases would result in a much older estimate than the true onset of cooling. For overdispersed data or grains that are uncharacterized, the youngest individual age can be treated as the sample's maximum cooling age (Murray et al., 2014). Following this approach, we find that the youngest individual grain ages for all samples in the SAZ range between 9.4 and 1.0 Ma (Table S1 and Figure 2). This is consistent with the mean reset ages ( $n = 11$ ), which are clustered between 7.1 and 1.6 Ma (Table 3 and Figure 5). Therefore, we interpret the mean reset AHe ages as relevant estimates for the timing of cooling through the AHe closure temperature in the SAZ. Mean ages young eastward, ranging from 5.6 to 7.1 Ma in the western SAZ, 3.4 to 4.0 Ma in the central SAZ, and 1.6 to 3.5 Ma in the eastern SAZ. At shallower stratigraphic levels, mixed reset and partial reset ages in the SAZ were obtained from Jurassic-Cretaceous to Oligocene rocks. In the western SAZ, the transition from fully reset to partial reset AHe ages occurs at burial depths between ~2.5 and 3.5 km, and in the central and eastern SAZ, this transition occurs at burial depths between ~5 and 6 km.

#### 4.4. Age-Depth Analysis

Age-depth analysis evaluates the apparent age pattern of thermochronologic data as a function of structural paleodepth using the concept of exhumed fossil partial retention and annealing zones (e.g., Gleadow et al., 1986; Stockli, 2005). We compiled published estimates of modern and paleogeothermal gradients across the EC, IAZ, and SAZ of southern Bolivia (Table 4) and take advantage of the well-defined fossil ZHe and AHe PRZ's exposed in the EC and SAZ (respectively) in order to estimate paleogeothermal gradients and depths

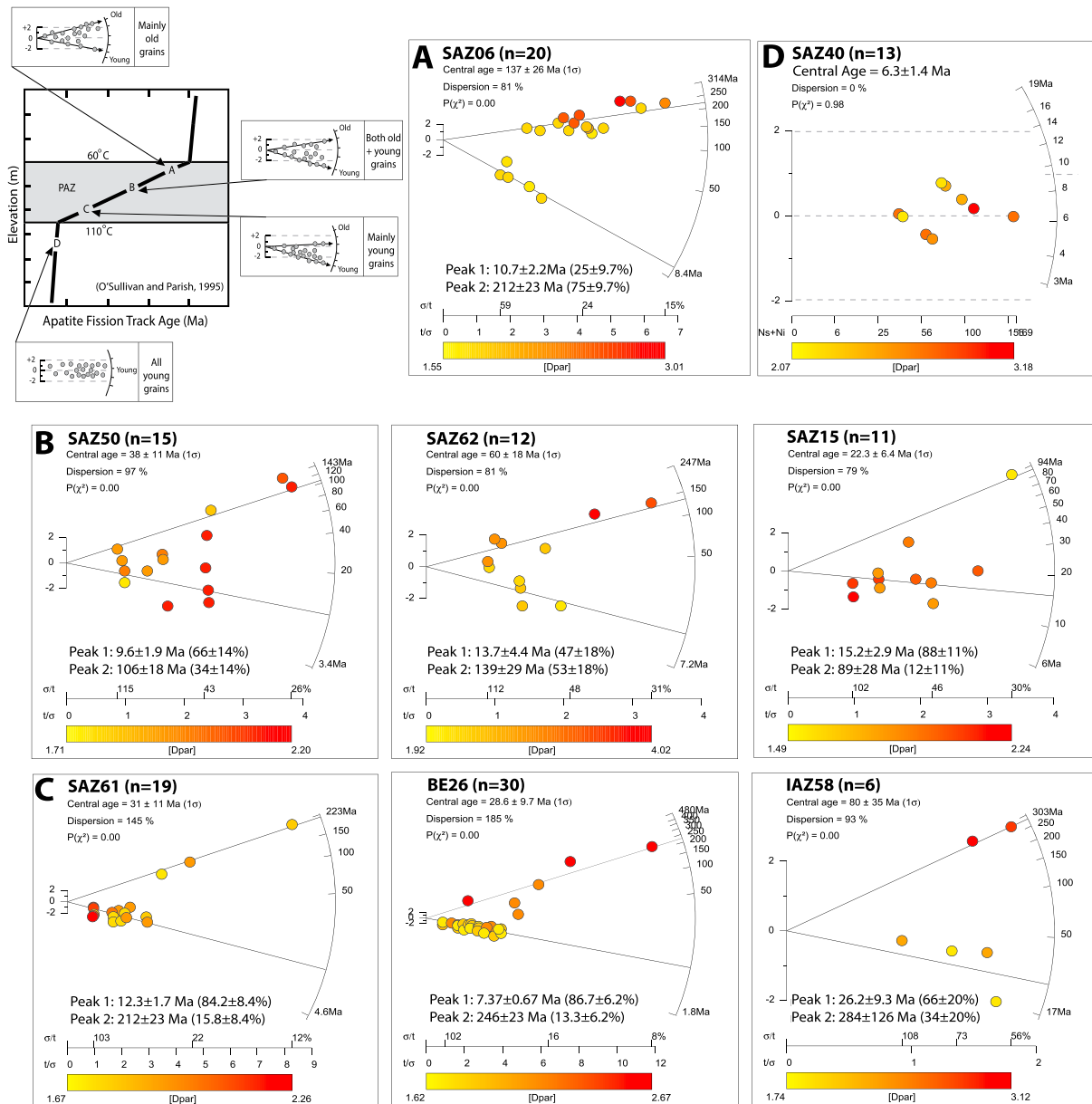


**Figure 6.** Radial plots of overdispersed apatite fission track (AFT) ages [ $P(\chi^2) < 5\%$ ] in the Subandean and eastern Interandean zones using RadialPlotter software (Vermeesch, 2009). Age-elevation graph from O'Sullivan and Parrish (1995) shows the idealized distribution of AFT grain ages on a radial plot depending on where it resided relative to the partial annealing zone (PAZ). Colored graphs show radial plots from this study along with measurements of grain  $D_{par}$ . (a) Sample SAZ06, characteristic of residence in the upper part of the PAZ. (b) Samples SAZ50, SAZ62, and SAZ15, characteristic of residence in the middle part of the PAZ. (c) Samples SAZ61, BE26, and IAZ58, characteristic of residence near the base of the PAZ. (d) Sample SAZ40, characteristic of complete annealing.

to the total annealing and total helium diffusion isotherms (e.g., Gleadow et al., 1986; Stockli, 2005). A detailed discussion of assumptions is included in the SI.

Based on proximal borehole measurements between  $20^\circ\text{S}$  and  $22^\circ\text{S}$ , the modern geothermal gradient in the EC is  $\sim 27 \pm 11$   $^\circ\text{C}/\text{km}$  (Table 4; Henry & Pollack, 1988). Published estimates of Oligocene paleogeothermal gradients in the EC (western EC:  $27.5 \pm 10.5$   $^\circ\text{C}/\text{km}$ ; eastern EC:  $23 \pm 8.5$   $^\circ\text{C}/\text{km}$ ) and IAZ ( $26 \pm 9$   $^\circ\text{C}/\text{km}$ ) fall within the range of modern estimates (Ege et al., 2007; Table 4). The modern geothermal gradient in the SAZ ranges between  $18 \pm 4$  (Henry & Pollack, 1988) and  $22 \pm 4$   $^\circ\text{C}/\text{km}$  (Springer & Forster, 1998), and depth profiles of AFT cooling ages across the SAZ at  $19.5^\circ\text{S}$  suggest a Miocene paleogeothermal gradient  $< 15$   $^\circ\text{C}/\text{km}$  (Barnes et al., 2008).

**Table 4**  
Geothermal Gradients (°C/km)

EC		SAZ			Time frame	Source
Western	Eastern	IAZ	Western	Eastern		
—	—	—	22 ± 4	—	Modern	Springer and Forster (1998)
27 ± 11	—	—	18 ± 4	—	Modern	Henry and Pollack (1988)
32–23 ± 6	19–27 ± 4.5	26 ± 9	—	—	Oligocene	Ege et al. (2007)
—	—	27 ± 11 <sup>a</sup>	< ~15	—	Mid-Miocene	Barnes et al. (2008)
—	27–23	—	24–14	10.5–14.5	Mid-to late-Miocene	This study

Note. Geothermal gradients are calculated using mean annual surface temperatures of 10 °C in the Eastern Cordillera (EC), 15 °C in the Interandean zone (IAZ), and 23 °C in the Subandean zone (SAZ; Instituto Geografico Militar, 2000; Springer & Forster, 1998).

<sup>a</sup>Temperature gradient is assumed to be similar to measurements in the EC.

In the eastern EC (Figure 7a), sample depths are plotted relative to the top of the Mesozoic-Cenozoic sedimentary section, which has a minimum measured thickness of 3.2 km in the Camargo syncline (DeCelles & Horton, 2003). Because there are no documented growth strata, and the wedge-top portion of the synorogenic rocks in the Camargo syncline has been eroded (DeCelles & Horton, 2003), depths shown in Figure 7a are minimum peak burial depths. The age-depth plot of the ZHe ages shows that the transition from reset to mixed reset ages occurs between 7.0 and 6.7 km. Using the range of paleoisotherms for the ZHe data (170–200 °C, see SI for a discussion of assumed paleoisotherms), the estimated preexhumational geothermal gradient in the eastern EC was ~27–23 °C/km, which is consistent with modern measurements and other paleogeothermal gradient estimates and is consistent with the unreset ZFT ages obtained from samples at ~9- to 11-km depths.

On age-depth profiles, the lower inflection point that defines the base of the fossil PRZ or PAZ can be interpreted as the age of onset of rapid exhumation (e.g., Gleadow et al., 1986; Stockli, 2005). In the eastern EC, the ~7-km depth to the base of the ZHe PRZ is well defined for samples collected across the Cuesta de Sama anticlinorium. However, the age of the inflection point cannot be precisely defined because three of the four deepest ZHe ages define an older inflection point at ~39–40 Ma, while the remaining five reset ZHe ages define an inflection point at ~28–30 Ma (Figure 7a). At depths <7 km, AHe and AFT ages are deflected toward younger ages. The overlap of AHe and AFT ages between ~7- and 3.2-km depths suggests a later stage of rapid exhumation between ~18 and 15 Ma.

Sedimentological data provide some constraints on the magnitude and timing of diachronous peak burial of samples in the SAZ (Figure 7b). In the western, central, and eastern SAZ, Neogene synorogenic rocks representing distal (~27–14 Ma Petaca Fm.) through proximal foredeep (~19–2 Ma Guandacay Fm.) deposits lack any evidence of growth strata (Calle et al., 2018; Uba et al., 2005, 2006, 2009) and are therefore inferred to have accumulated prior to active thrusting in each thrust sheet. Thus, the age-depth plots are graphed relative to the top of the preserved Guandacay Formation, and total burial depths determined from the restored position of each sample on Figure 5 are assumed to be the minimum peak burial depths. The timing of peak burial in the western SAZ is inferred to closely follow the maximum onset of deformation, which occurred between ~19 and 9 Ma in the adjacent thrust sheet to the east (Calle et al., 2018), and the ~9–8 Ma minimum age of the Guandacay Formation in the eastern IAZ-western SAZ (Hulka, 2005; Uba et al., 2009). In the eastern SAZ, peak burial and exhumation can be constrained between a  $3.8 \pm 0.1$  Ma ash horizon near the top of the Guandacay Formation within the immediate footwall of the Mandiyuti Thrust (Figure 5, central eastern SAZ boundary; Calle, 2013) and ~2 Ma growth strata between the Guandacay Formation and overlying Emborozu Formation to the east of the frontal anticline (Uba et al., 2009). The peak burial timing of the central SAZ is therefore inferred to have occurred at sometime between ~8 and 3.8 Ma.

Plotting AHe age-depth by individual thrust sheet, it appears that the paleogeothermal gradient differs across the SAZ (Figure 7b). In the western SAZ, the depth to the lower inflection point is ~3.6 km below the top of the Neogene section, and ~6 km in the central and eastern SAZ. In all three SAZ thrust sheets there is an ~1- to 1.5-km gap between the AHe ages that define the lower and upper inflection points, and it is uncertain whether the AHe PRZ was moving or static before exhumation (e.g., Berner, 2009). Therefore, a range of possible paleogeothermal gradients is determined by assuming that the 85 °C paleoisotherm was

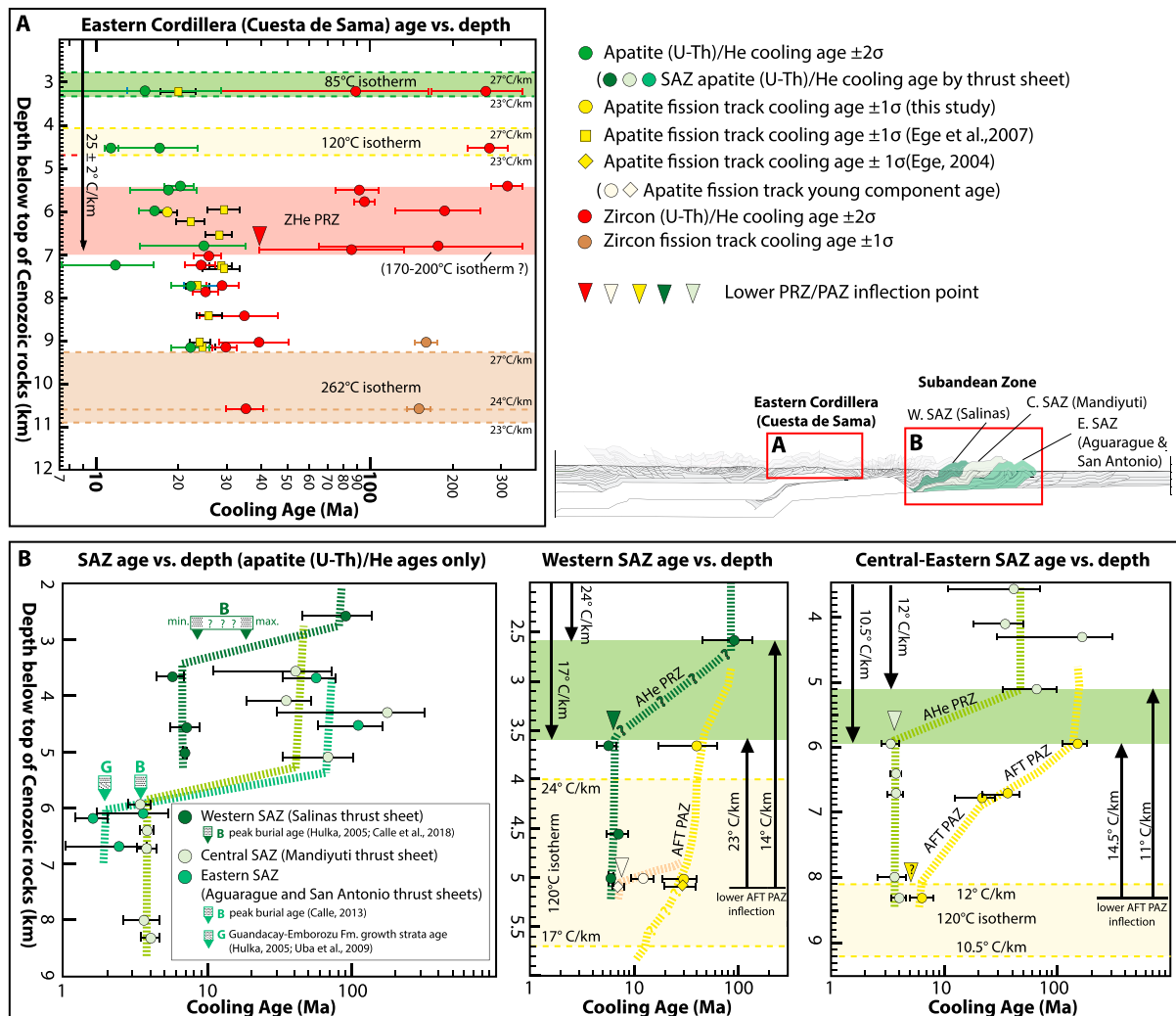


**Figure 7.** Cooling ages plotted against preexhumational paleodepth relative to the top of Cenozoic rocks. Relative depths used for preexhumational geothermal gradient calculation shown with black arrows. (a) Age-depth plot of cooling ages in the eastern Eastern Cordillera (Cuesta de Sama anticlinorium) showing a well-defined inflection point at a paleodepth of  $\sim 7$  km for ZHe data. (b) Age-depth plot of cooling ages in the Subandean zone (SAZ) that show well-defined inflection points for AHe data at differing depths between the western SAZ and central eastern SAZ. Geothermal gradient calculations are estimated from the depth difference between the top of the Cenozoic section and the possible range of the AHe partial retention zone (PRZ), as well as the depth difference between the AHe PRZ and apatite fission track (AFT) partial annealing zone (PAZ).

located at any depth between the reset to unreset ages. Using these constraints, a 17–24 °C/km paleogeothermal gradient range is estimated for the western SAZ, and 12–10.5 °C/km is estimated for the central and eastern SAZ (Table 4 and Figure 7b). The AFT data show that the deepest samples in the SAZ are located within the proposed 120 °C paleoisotherm ranges constructed from the AHe PRZ (Figure 7b) and may be interpreted as the maximum depth to the lower inflection point of the AFT PAZ. The paleogeothermal gradient can also be estimated by comparing the relative difference in depth and the 35 °C temperature difference between the AHe PRZ and AFT PAZ (e.g., Stockli et al., 2002), which yields 23–14 °C/km for the western SAZ and 14.5–11 °C/km for the central eastern SAZ, which are consistent with the AHe PRZ values listed above.

Crustal thermal gradients in an orogen are likely to evolve through time due to redistribution of mass by erosion and sedimentation (Ehlers, 2005). The geothermal gradients in the SAZ are expected to be lower than in the EC-IAZ because development of the foreland basin and sedimentation on the eastern flank of the mountain belt since the early Miocene should have advected cooler surface temperatures downward (e.g., Ehlers,



2005). However, the significant difference in the paleogeothermal gradients between the western SAZ and central eastern SAZ over such a short horizontal distance should be viewed with caution because the samples were not collected from a true vertical transect and thus may be subject to local variation due to topographic effects (e.g., Reiners et al., 2015), and there is some uncertainty associated with unknown original stratigraphic thickness immediately above each sample location. Nevertheless, the range of values for the western SAZ (24–14 °C/km) do partially overlap with the lower temperature values in the central eastern SAZ (14.5–11 °C/km) and therefore provide a broad but useful constraint for peak burial conditions in the thermal models discussed below.

The age of the inflection point is subject to far less uncertainty from transient topography than the depth to the inflection point on an age-depth analysis (e.g., Stockli et al., 2002). Thus, the more important finding from the age-depth profiles is the onset time of uplift and erosion in each major thrust sheet in the SAZ, which provides information on the rate of propagation of the deformation front. In the western SAZ, the onset of rapid exhumation defined by the ~3.5-km-deep AHe PRZ inflection point is interpreted at ~7 Ma, consistent with the suggested ~7- to 10-Ma PAZ inflection point inferred by the AFT young component ages at ~5-km depth. In the central SAZ, the ~6-km-deep AHe PRZ inflection point is interpreted at ~4 Ma, and the ~8-km-deep AFT PAZ inflection point is defined by a  $6.3 \pm 1.5$ -Ma reset AFT age from the deepest structural level. In the eastern SAZ, the ~6-km-deep AHe inflection point is interpreted at ~2 Ma.

#### 4.5. Thermal Modeling

Sample data that best represent each tectonomorphic zone were inverse modeled to provide more quantitative estimates of the onset of rapid exhumation and cooling rates. We used the program HeFTy (Ketcham, 2005), which employs a Monte Carlo approach to generate a large number of time-temperature ( $t$ - $T$ ) cooling paths from which thermochronologic data are predicted according to published FT annealing and He diffusion models (see SI for detailed methods and model parameters). The resulting predicted data for each  $t$ - $T$  path are compared to the measured cooling ages of each individual sample and reported as envelopes classified as *good* (0.5) or *acceptable* (0.05) using a probability of fit calculated with a Kuiper's statistical test (Ketcham, 2005). We manually impose constraints on the peak burial conditions in each model because allowing the inverse model to solve for the peak burial conditions often resulted in predicted  $t$ - $T$  paths that violated known geologic and thermal constraints from sedimentological data, age-depth profiles, and the reset and unreset thermochronologic ages in a particular sample. The timing of peak burial prior to exhumation in each model was determined from published sedimentological constraints (e.g., Calle, 2013; Calle et al., 2018; Elger et al., 2005; Horton, 2005; Hulka, 2005; Uba et al., 2006, 2009). The peak burial temperature conditions were calculated using the depth of the sample below the top of the Cenozoic section and the range of paleogeothermal gradients in Table 4.

In the EC, we modeled samples ECO61/EC81 and ECO35/EC30 from the Cuesta de Sama anticlinorium, and sample ECO293/EC64 at the EC-Altiplano boundary (Figure 8a). Good fit  $t$ - $T$  paths show that sample ECO61/EC81 cooled rapidly (~10 °C/Myr) from >~180 °C beginning at 43–32.5 Ma, followed by more moderate cooling (~4 °C/Myr) after ~25 Ma. Good fit  $t$ - $T$  paths for the adjacent sample ECO35/EC30 show rapid cooling (~11 °C/Myr) from >~145 °C beginning at 33–28 Ma, followed by slow cooling (3 °C/Myr) after ~22–20 Ma. For sample ECO293/EC64, good fit  $t$ - $T$  paths show rapid cooling (~21 °C/Myr) from ~150 to 80 °C starting at ~29–27.5 Ma, followed by slower cooling (~2 °C/Myr) after ~20 Ma.

Samples ECO-IAZ03 from the EC-IAZ boundary and IAZ13 from the central IAZ were modeled (Figure 8b). The good fit  $t$ - $T$  paths for sample ECO-IAZ03 showed rapid cooling (~13 °C/Myr) from >~147 °C starting at ~25–18.5 Ma, followed by moderate to slow cooling (~4 °C/Myr) from ~97–21 °C to surface temperatures after ~17.5–15 Ma. Sample IAZ13 shows rapid cooling (~15 °C/Myr) from >~90 °C beginning at ~19.5–17 Ma, followed by moderate to slow cooling (3 °C/Myr) from ~45 °C after ~14–7 Ma. In the eastern IAZ, we modeled (from west to east) samples IAZ11, IAZ347, and IAZ58 (Figure 8b). No good fit  $t$ - $T$  paths were found for IAZ11, but acceptable fit paths show that this sample underwent rapid cooling (8–9 °C/Myr) from >~90 °C beginning at ~10–11 Ma. Good fit  $t$ - $T$  paths for sample IAZ347 are consistent with IAZ11 and show rapid cooling (~9 °C/Myr) from >~80 °C beginning between ~15 and 10.5 Ma. For sample IAZ58, located at the IAZ-SAZ boundary, good fit paths define slow cooling (4 °C/Myr) from >~70 °C as early as ~14 Ma, with rapid cooling (9 °C/Myr) from >~62 °C starting at ~9.5–7 Ma.

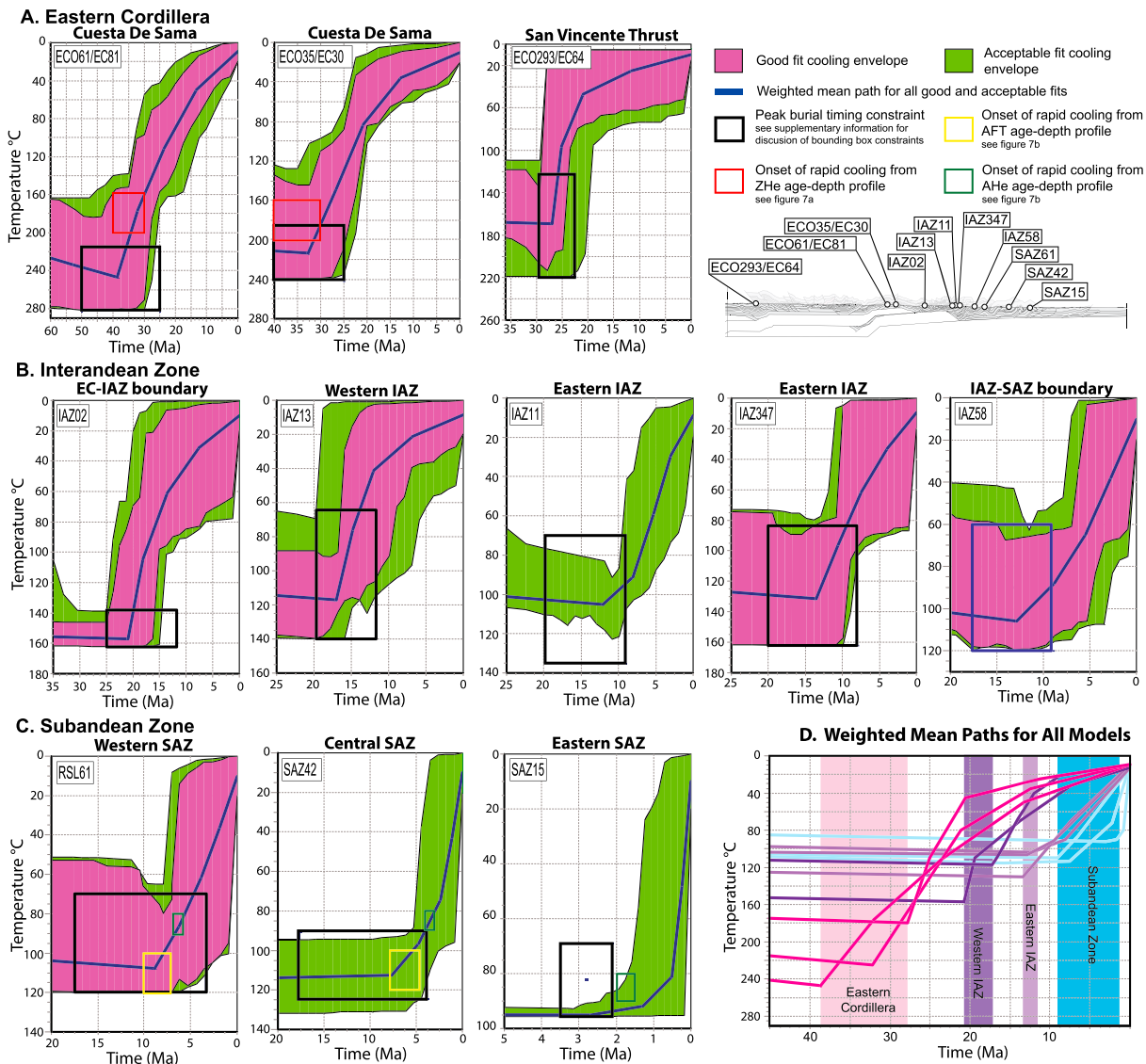


**Figure 8.** Inverse models of  $t$ - $T$  cooling envelopes (modeled in HeFTy; Ketchum, 2005) for samples in the (a) Eastern Cordillera, (b) Interandean zone (IAZ), and (c) Subandean zone (SAZ). Peak burial constraints were calculated from burial depths on the restored cross sections and the geothermal gradients in Table 4. Where available, modeled cooling envelopes are compared to the onset of rapid cooling estimated from age-depth profiles. (d) Compiled weighted mean paths for all models grouped by tectonomorphic zone: pink = EC, dark purple = western IAZ, light purple = eastern IAZ, and blue = SAZ.

Samples SAZ61, SAZ40, and SAZ15 were modeled from the western, central, and eastern SAZ, respectively (Figure 8c). For SAZ61 and SAZ15, no  $t$ - $T$  paths could be found when the partially reset AFT data were included in the inverse model, so only the AHe data were modeled in these two samples. Good fit  $t$ - $T$  paths show that SAZ61 cooled rapidly (11 °C/Myr) from  $>65$  °C beginning at  $\sim 7$ –8 Ma. Acceptable paths show that SAZ40 cooled rapidly ( $\sim 9$  °C/Myr) from  $>90$  °C starting at 6.1–5.3 Ma and that SAZ15 began slow cooling ( $\sim 3$  °C/Myr) from  $\sim 90$  to 98 °C beginning by  $\sim 2.5$  Ma and cooled rapidly ( $>100$  °C/Myr) from  $\sim 90$  °C after  $\sim 1.5$  Ma.

The best fit  $t$ - $T$  paths generated using HeFTy are consistent with the general distribution of reset ages observed across the thrust belt (Figure 2) and are in good agreement with the estimates for the onset of rapid exhumation determined from age-depth analysis (Figure 7). Comparison of the weighted mean cooling paths for all models (Figure 8d) illustrates the general onset of exhumation at  $\sim 40$  Ma in the EC and the overall eastward younging of the onset of rapid cooling as the thrust belt advanced toward the foreland, as well as the progressive eastward decrease in peak temperature that samples were exhumed from.

**Table 5**  
Summary of Refined Deformation Chronology

Constraint (Ma)	Altiplano			Eastern Cordillera			Interandean zone			Subandean zone			Chaco
	Western central	Eastern	Western	Central	Eastern	Western	Eastern	Western	Central	Eastern			
Mean cooling ages	17.9–33.1 <sup>b</sup>	27.7–21.5 <sup>a,b</sup>	31.5–36.7 <sup>a,b</sup>	39.2–24.1 <sup>a</sup>	~40–28 <sup>a</sup>	19–15.1 <sup>a</sup>	11.1–8 <sup>a</sup>	12.3–7.4 (VC) <sup>a,c</sup>	6.3 ± 1.5 <sup>a</sup>	2.4–1.6 <sup>a</sup>			
Age-depth analysis	—	—	—	—	~40–28 <sup>a</sup>	—	—	~10–7 <sup>a</sup>	~6.3–4 <sup>a</sup>	~2 <sup>a</sup>			
Modeled cooling age	—	—	~29–27.5 <sup>a</sup>	~40–36 <sup>b</sup>	~43–32.5 <sup>a</sup>	~25–17 <sup>a</sup>	~11–7 <sup>a</sup>	~7–8 <sup>a</sup>	6.1–5.3 <sup>a</sup>	2.5–1.5 <sup>a</sup>			
Sedimentological	~19–8 <sup>d</sup>	~30–27 <sup>d</sup>	~30–27 <sup>d</sup>	>25 <sup>h</sup>	>25 <sup>h</sup>	<25 <sup>h</sup>	~19–9 <sup>e</sup>	<12 <sup>g</sup>	—	<2.1 <sup>f,g</sup>	>0 <sup>g</sup>		
Used in forward model (Figure 9)	~19–10	~30–27	~30–27	~40–36 (~26–21, ~16–10 (J,K,L))	~43–40	~25–17	~11–8	~8–6	—	2–1.5	1.5–0		

Note. Constraints from mean cooling ages: **red** = ZHe, **yellow** = apatite fission track (AFT), and **green** = AHe. <sup>a</sup>Gray = (out of sequence phase). <sup>b</sup>Bold: age constraints used in the forward model. <sup>c</sup>This study. <sup>d</sup>Ege et al. (2007). <sup>e</sup>Ege (2004). <sup>f</sup>Elger et al. (2018). <sup>g</sup>Uba et al. (2009). <sup>h</sup>Horton (2005). <sup>i</sup>Gubbels et al. (1993). <sup>j</sup>Hérail et al. (1996). <sup>k</sup>Horton (1998). <sup>l</sup>Müller et al. (2002).

Note. Constraints from mean cooling ages: red = ZHe, yellow = apatite fission track (AFT), and green = AHe. Gray = (out of sequence phase). Bold: age constraints used in the forward model. <sup>a</sup>This study. <sup>b</sup>Ege et al. (2007). <sup>c</sup>Ege et al. (2004). <sup>d</sup>Elger et al. (2005). <sup>e</sup>Calle et al. (2018). <sup>f</sup>Hulkla (2005). <sup>g</sup>Uba et al. (2009). <sup>h</sup>Horton (2005). <sup>i</sup>Gubbels et al. (1993). <sup>j</sup>Hérail et al. (1996). <sup>k</sup>Horton (1998). <sup>l</sup>Müller et al. (2002).

## 5. Refined Deformation Chronology

The cooling ages presented here build upon an existing chronologic framework for deformation across the Andean retroarc and refine the timing of deformation-driven exhumation in the IAZ and SAZ, where published constraints are minimal (Table 5). Initial Andean deformation was focused along the western margin of the South American continent beginning between ~100 and ~70 Ma (Arriagada et al., 2006; Bascuñán et al., 2016; Horton, 2018b) but made a major eastward jump into the EC by the Eocene (e.g., DeCelles & Horton, 2003; McQuarrie et al., 2005; Sempere et al., 1997). Initiation of deformation in the eastern EC between ~43 and 40 Ma is supported by reset ZHe ages as old as ~39 Ma, onset of exhumation at ~40 Ma interpreted from age-depth analysis, and thermal modeling that shows rapid cooling beginning possibly as early as ~43 Ma. Following this, deformation propagated westward through the central EC between ~40 and 36 Ma (Ege et al., 2007) and reached the EC-Altiplano boundary (San Vicente thrust) by ~29–27.5 Ma (Figure 8a). This east to west progression of accelerated cooling is consistent with the model of backthrust development via tectonic wedging of a basement thrust sheet that has been proposed for the central Andes (e.g., Anderson et al., 2017; Horton, 2005; McQuarrie, 2002; Rak et al., 2017).

Diminished deformation in the EC and eastward migration of the thrust front into the IAZ was inferred by a transition from foredeep sedimentation to development of intermontane basins in the central and western EC after ~25 Ma (Horton, 2005). This is consistent with our thermal modeling of samples in the EC, which show a change from rapid (~24–10 °C/Myr) to slow cooling rates (~2–4 °C/Myr) after ~25–20 Ma, and the onset of rapid cooling in the western IAZ beginning between ~25 and 18.5 Ma. Development of Oligocene-Miocene intermontane basins and ~26–21 Ma AFT ages in the central and western EC record out-of-sequence deformation that began by ~26 Ma (Ege et al., 2007; Horton, 2005) and was completed prior to the ~12–10 Ma development of the San Juan del Oro erosional surface (Gubbels et al., 1993; Hérail et al., 1996; Kennan et al., 1997; Horton, 1998; Müller et al., 2002). Thus, our ~20–12 Ma AHe ages from the central and western EC reflect the waning stages of out-of-sequence deformation, as they predate the ~12–10 Ma San Juan del Oro erosion surface. Sequential restoration of deformation in the central and western EC indicates that a second, out of sequence phase of shortening occurred between ~15.7 and 10 Ma (Anderson et al., 2017), consistent with the majority of our AHe ages in this region, which range from 15.2 to 12.1 Ma.

The across-strike distribution of AFT ages illustrates two periods of widespread cooling and eastward migration of the deformation front, with ~19–15 Ma ages limited to the western IAZ and ~11–8 Ma ages in the eastern IAZ. Our thermal modeling shows that rapid cooling began at the western margin of the IAZ by 25–18.5 Ma and reached the central IAZ by 19.5–17 Ma. Migration of rapid cooling from the EC into the IAZ may also be reflected by the shallower AHe and AFT samples on the age-depth profile of the Cuesta de Sama anticlinorium, which show a later stage of rapid exhumation between ~18 and 15 Ma (Figure 7a). Eastward migration of rapid cooling defined by the AFT ages in the central IAZ apparently paused for ~6 Myr, but resumed by ~11–10 Ma and reached the IAZ-SAZ boundary by ~9.5–7 Ma. Though the across-strike trend of AHe ages from the central IAZ to the western SAZ are more continuous, a steep age versus distance trend (Figure 2) is consistent with diminished eastward propagation of the thrust front (e.g., Reiners et al., 2015; Thomson et al., 2010) over a similar ~6-Myr time frame. This is consistent with rapid forward propagation of the thrust belt at 11 ± 3 Ma inferred from thermochronologic data at ~20°S (Lease et al., 2016).

Further to the west, in the Altiplano, Cenozoic sedimentary rocks and AFT ages record two phases of thrust faulting that occurred at ~30–27 and 19–10 Ma (Ege et al., 2007; Elger et al., 2005). The first phase of shortening coincided with the westward migration of cooling across the EC, and the second phase was synchronous with the period of distributed, out-of-sequence shortening in the EC and the eastward migration of cooling across the IAZ. Though 85% of the total shortening accommodated in the Altiplano occurred during the younger phase, the majority of deformation was accomplished before ~10 Ma (Elger et al., 2005), coinciding with development of the San Juan del Oro erosional surface.

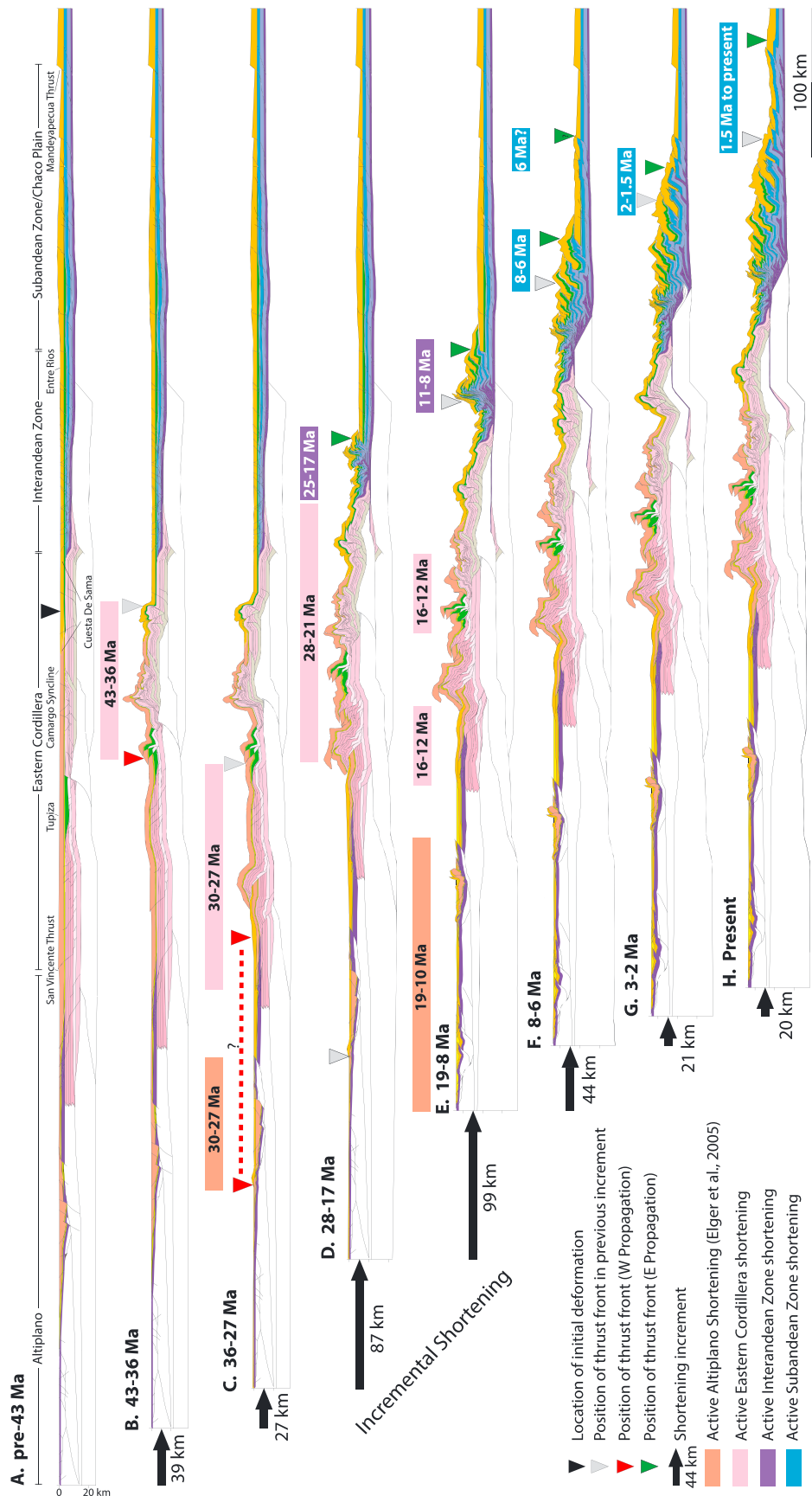


**Figure 9.** Sequential restoration of cross-section A-A', showing the kinematic evolution of the central Andean thrust belt at ~21°S modeled using 2D Move (Midland Valley). Restored sections from the Altiplano (Elger et al., 2005) and Eastern Cordillera, Interandean zone, and Subandean zone (Anderson et al., 2017) are forward modeled in eight steps. Colored bars above sections show region and timing of active shortening interpreted from modeled cooling ages (Figure 8).



Our modeling and inflection points from age-depth analysis show that rapid cooling began at ~8–7 Ma in the western SAZ, and at ~6.3–5 Ma in the central SAZ. In the eastern SAZ, stratigraphic growth relationships between the Guandacay Formation and the overlying Emborozu Formation on the eastern flank of the topographic front indicate active shortening in the frontal-most anticline after ~2.1 Ma (Hulka, 2005; Uba et al., 2009). Our modeling and age-depth data are in agreement with this estimate and show that rapid cooling began between ~2 and 1.5 Ma. Growth relationships documented in seismic reflection profiles indicate minor out-of-sequence shortening between ~6 and 2.1 Ma on a blind thrust fault located east of the topographic front (Horton & DeCelles, 1997; Uba et al., 2009). However, the majority of shortening and thrust propagation between the modern topographic front and the active thrust front (Mandeyapecua thrust; Figure 1) occurred after 2.1 Ma (Brooks et al., 2011; Costa et al., 2006; Uba et al., 2009).

## 6. Shortening and Propagation Rates From Cross Section Forward Modeling

Using the deformation timing constraints discussed above (summarized in Table 5), we performed forward modeling of the cross section using the program Move (Midland Valley), in order to track cumulative shortening and the thrust front position through time (Figure 9). The model was constructed from the balanced and restored cross section in Anderson et al. (2017), and based on the kinematics of basement thrust sheet emplacement summarized in section 2.2 in this paper. The cross section is deformed using the fault parallel flow and trishear algorithms in Move (e.g., McQuarrie, Barnes, & Ehlers, 2008), but isostatic loading and topography were not accounted for in our sequential models. The forward model is shown in eight sequential steps defined by the revised deformation chronology (Table 5), though some steps include multiple phases of deformation when the order of shortening in different sectors of the thrust belt is not resolved individually because of chronological overlap (e.g., Figure 9e: 19–8 Ma Altiplano shortening, 16- to 12-Ma EC shortening, and 11- to 8-Ma IAZ shortening). Shortening magnitude was measured using the change in length of the cross section between each subsequent increment of deformation, whereas propagation magnitude was determined by measuring the distance that the thrust front migrated in each step. We used the range of timing estimates within each zone discussed in the preceding section to assign a general error bound for each point on the graph (Figures 10a and 10b) and then calculated rates with formal errors in Isoplot (Ludwig, 2012) using a robust linear regression (including a  $\pm 10\%$  uncertainty for shortening and propagation magnitudes) when more than two age constraints were available (Figure 11). When only two age constraints were available, a rate with symmetric errors was found using the maximum and minimum bounds of the timing estimate (Figure 10). Though shortening magnitudes are shown by individual tectonic zone (Figure 10a), we only assigned error to the cumulative shortening graph because it is easier to determine when shortening was accomplished in zones with overlapping deformation chronologies and attribute error bounds (e.g., all Altiplano and EC deformation complete by  $10 \pm 2$  Ma).

Although the shortening and thrust front propagation rates vary through time (Figure 11), a few general trends stand out on the cumulative shortening and thrust front propagation graphs (Figures 10a and 10b). After ~27 Ma, the shortening rate is double that of the earlier history of the thrust belt (Figure 10a). Trends in thrust front propagation can be divided into three major phases (Figure 10b): (1) an early period of rapid westward propagation from ~43 to 27 Ma, (2) a period of slower eastward propagation from ~25 to 17 Ma, and (3) a period of rapid eastward propagation that began at ~11 Ma and persists to the present.

In detail, deformation initiated in the Cuesta de Sama anticlinorium at ~43–40 Ma and propagated westward to the EC-Altiplano boundary by ~27 Ma, first at a rate of  $14.1 + 2.1/-1.1$  mm/year, then increasing to  $37.6 + 11.9/-6.1$  mm/year (Figures 9a–9c and 11). Shortening rates during this period were slow, at  $4.5 + 0.9/-0.5$  mm/year. Between ~28 and 17 Ma (Figure 9d), shortening rates increased to  $8.4 + 4.5/-0.4$  mm/year, as shortening was accommodated in the EC from ~28 to 21 Ma and in the IAZ from ~25 to 17 Ma. During the first phase of out of sequence shortening in the EC (~28–25 Ma), propagation rates decreased, likely to rates  $< 5$  mm/year. The onset of deformation in the IAZ marked the renewal of the eastward advance of deformation, with the thrust front propagating from the Cuesta de Sama anticlinorium to the central IAZ at a rate of  $16.1 + 2.5/-1.3$  mm/year.

Following the first phase of IAZ deformation (Figure 9e), propagation rates fell to zero as the eastward advance of the thrust front stalled in the central IAZ from ~17 to 11 Ma. This is consistent with early to

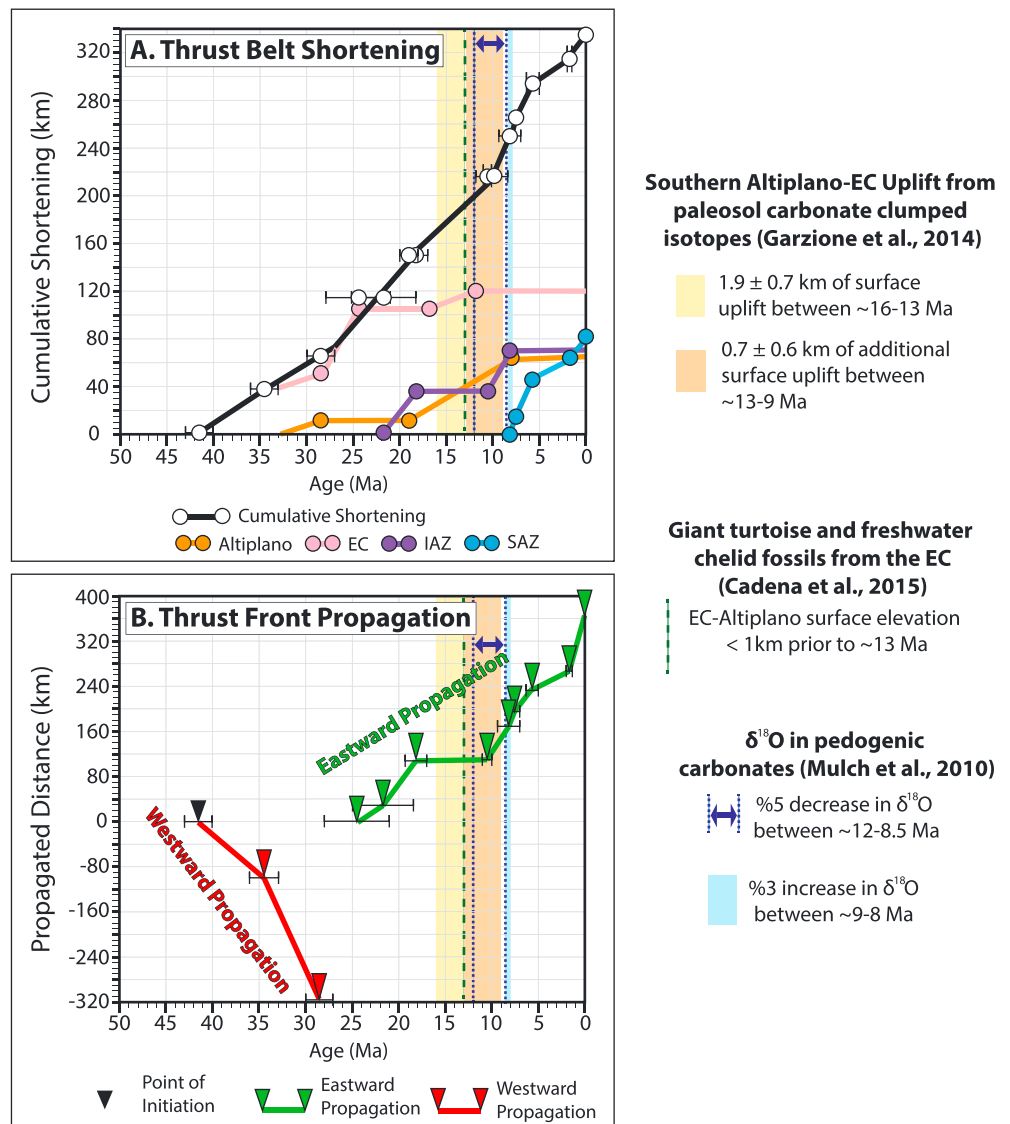


**Figure 10.** Graphs of (a) cumulative thrust belt shortening, and (b) propagated distance of the thrust front. Paleoclimate and paleoelevation data shown at bottom of figure are the same for Figures 10–12. EC = Eastern Cordillera; IAZ = Interandean zone; SAZ = Subandean zone.

middle Miocene stalling of forward deformation inferred from thermochronologic data in central and northern Bolivia (Barnes et al., 2006, 2008; McQuarrie, Barnes, & Ehlers, 2008). Shortening rates decreased slightly during this period to  $7 \pm 3.5$  mm/year as  $\sim 55$  km of out-of-sequence shortening was accommodated in the Altiplano between  $\sim 19$  and 8 Ma, and a final  $\sim 12$ – $15$  km of shortening was accommodated in the western EC between  $\sim 16$  and 12 Ma. Eastward advance of the thrust front resumed at  $\sim 11$  Ma (Figure 9e), propagating from the central IAZ to the IAZ–SAZ boundary by  $\sim 8$  Ma at a rate of  $27.8 + 1.2/-0.6$  mm/year, concurrent with an increase in shortening rate to  $15.4 + 10.5/-0.3$  mm/year.

After  $\sim 10$ – $8$  Ma, all hinterland deformation ceased and the locus of shortening was focused along the eastern flank of the mountain belt (Figures 9f–9h). Between  $\sim 8$  and 6 Ma (Figure 9f), thrust front propagation decreased to  $20.9 + 1.5/-0.7$  mm/year as deformation propagated through the western and central SAZ, but shortening rates remained steady at  $15.4 + 10.5/-0.3$  mm/year. Growth strata interpreted from seismic imagery indicate that the thrust front made a major eastward jump to the La Vertiente fault (Figure 5) at  $\sim 6$  Ma (Uba et al., 2009). However, this eastward advance was likely a transient event given the low

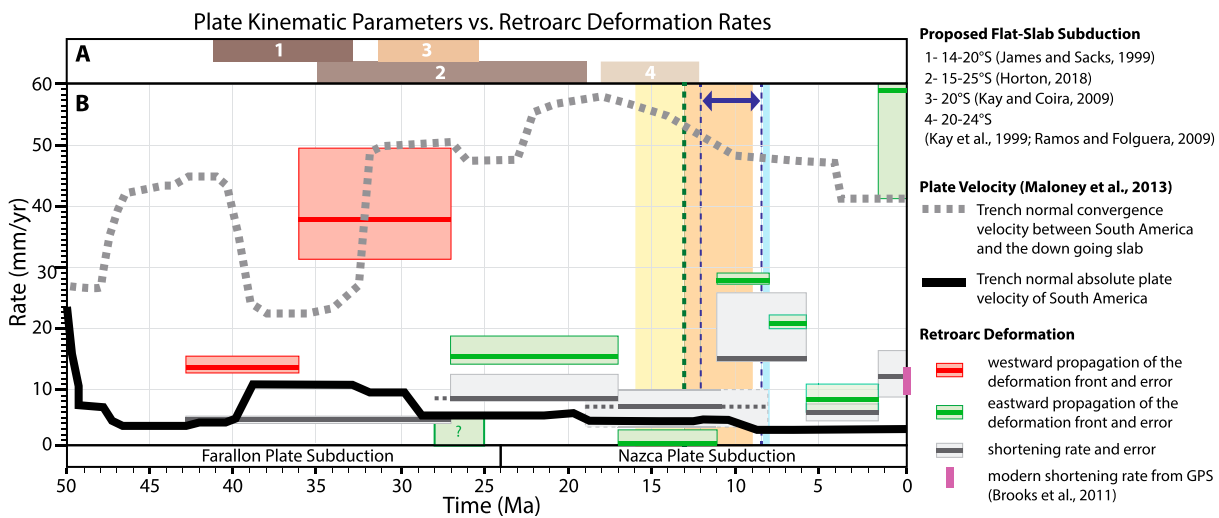


**Figure 11.** Plate kinematic parameters graphed against retroarc deformation. (a) Periods of flat-slab subduction proposed for the central Andes (15–25°S). (b) Trench-normal convergence velocity between South America and the Nazca slab and trench-normal absolute plate velocity of South America compared to calculated retroarc shortening rates and thrust front propagation rates.

magnitude of shortening accommodated by the La Vertiente fault (Figure 9f). Following this, deformation then retreated to the west as our thermal models show onset of rapid cooling in the central SAZ between 6.3 and 5 Ma. Eastward migration of the thrust front from the central to the eastern SAZ continued between ~5 and 1.5 Ma (Figure 9g) but slowed to a rate of  $8.5 \pm 2.5$  mm/year, with shortening rates decreasing to  $6 \pm 1.7$  mm/year. After ~1.5 Ma (Figure 9h), the propagation rate increased significantly to  $59 \pm 17$  mm/year as the deformation front migrated ~90 km eastward across the Chaco Plain to the presently active Mandeyapeuca thrust. Shortening rates increased to  $12.4 \pm 3.6$  mm/year, which are consistent with modern shortening rates of 9–13 mm/year determined from GPS measurements (Brooks et al., 2011).

## 7. Discussion

### 7.1. Influence of Plate Interactions

Crustal shortening and associated thickening of the South American Plate is ultimately tied to the degree of coupling at its interface with the subducted oceanic plate (e.g., Dewey & Bird, 1970; Jordan et al., 1983; Lamb and Davis, 2003). The trench-normal absolute plate velocity of the South American continent likely exerts a first-order influence on plate coupling, and therefore on the tectonic mode along the entire plate margin (e.g., compression, extension, or stasis), whereas differences in slab dip at individual segments in the orogen may result in second-order spatial and temporal variability in horizontal shortening and arc magmatism (e.g., Coney & Evenchick, 1994; Horton, 2018a; Maloney et al., 2013; Oncken et al., 2006; Ramos, 2009; Ramos & Folguera, 2009). In Figure 11, we compare our calculated propagation and shortening rates for the retroarc with the published trench-normal absolute plate velocity of South America as well as the trench-normal convergence rate between South America and the subducting plate (~19°S) determined from a global kinematic plate model (Maloney et al., 2013) to elucidate any link between plate interaction and the observed variability in upper plate deformation.

Overall, the variation in retroarc shortening rates does not appear to be directly correlated with changes in either the trench-normal plate velocity of South America or the convergence rate between South America and the subducting slab (Figure 11). However, the major eastward jump of retroarc shortening into the EC does correspond with a substantial increase in trench-normal absolute plate velocity of South America and substantial decrease in trench normal convergence velocity at ~40 Ma. Thrust front propagation rates show even less relation to plate kinematic parameters, except for a decrease in trench-normal absolute velocity of South America that roughly corresponds in time with the switch from westward to eastward thrust front propagation at ~27 Ma.

Flat slab subduction events between ~25 and 15°S are inferred primarily from periods of cessation or lulls in magmatism and/or eastward migration of arc magmatism (James & Sacks, 1999; Kay et al., 1999; Kay & Coira, 2009; Ramos & Folguera, 2009). The phases of rapid eastward propagation of the deformation front in our new record do not directly correspond to any of the proposed periods of flat slab subduction in the central Andes, and lack the structural characteristics observed in modern flat slab regions (e.g., Ramos & Folguera, 2009). However, the early flat or shallow slab periods proposed at ~40–32 Ma (Horton, 2018a; James & Sacks, 1999; Kay & Coira, 2009) are contemporaneous with the major eastward jump in retroarc deformation and may explain the upper plate stress conditions that favored advancement of the deformation front into the EC rather than the rheologically weak Altiplano (e.g., Beck & Zandt, 2002).

These observations are consistent with recent compilations of upper plate deformation, which also show an unclear link between plate convergence rates and orogenic wedge propagation or shortening rates in the central Andes (DeCelles et al., 2015; Maloney et al., 2013; Oncken et al., 2006). However, the middle Eocene to earliest Miocene phase of flat slab subduction in the central Andes may have influenced the orogen-scale compressional tectonic regime and sustained upper plate shortening that promoted early development of wedge taper (e.g., Horton, 2018a; Ramos, 2009) but does not display a clear link to variable shortening and propagation rates in the upper plate.

## 7.2. Implications of Shortening and Propagation Rates for Evolution of the Andean Orogenic Wedge

The lack of correlation between upper plate deformation and the kinematics of the subducting plate does not preclude the fundamental influence that plate interaction has on orogenesis but does suggest that processes operating within the upper plate may play an important role in thrust belt evolution, at least in the central Andes (e.g., DeCelles et al., 2009, 2015). Therefore, here we interpret the deformation history of the thrust belt in the context of wedge dynamics. A critically tapered wedge is a steady state system, subject to transient perturbations to that state (Dahlen, 1990). Factors such as variation in décollement or wedge strength (e.g., Davis et al., 1983; DeCelles & Mitra, 1995; Wojtal & Mitra, 1986), basin geometry and structural inheritance (Allmendinger et al., 1983; Boyer, 1995), erosional and climatic effects (e.g., Willett, 1999; Horton, 1999; McQuarrie, Barnes, & Ehlers, 2008), or isostatic adjustment in response to buildup and removal of dense lower lithosphere (e.g., DeCelles et al., 2009, 2015; Garzione et al., 2006) may influence deformation by either altering the critical taper angle or perturbing the mass balance of the wedge (Dahlen, 1990; Whipple, 2009; Whipple & Meade, 2006). Overall, the shortening rate within the thrust belt should be equal to the convergence rate of the foreland crust (DeCelles & DeCelles, 2001), which itself controls the rate of accretionary influx of material into the wedge (Willett, 1999). In contrast, the propagation rate of the deformation front fluctuates with changes in wedge width (e.g., Reiners et al., 2015). If the wedge is critical and thus growing or shrinking self-similarly, changes to wedge width, and hence, shortening and propagation rate reflect a perturbation in the mass balance between accretionary influx ( $F_A$ ) and erosional efflux ( $F_E$ ), or a change in the wedge and/or detachment strength (Roe & Brandon, 2011; Stolar et al., 2006; Whipple, 2009; Whipple & Meade, 2006). For example, increasing  $F_E$  efficiency as  $F_A$  remains constant should result in wedge shrinkage or reduced wedge growth and correspond to a decrease in forward propagation rates relative to internal shortening of the wedge in order to maintain taper, whereas increasing  $F_A$  as  $F_E$  remains constant should result in wedge growth and an increase in forward propagation rates relative to internal deformation of the wedge, even as overall shortening rates increase (e.g., Whipple & Meade, 2006). Because we do not measure  $F_E$  directly, we interpret the state of the Andean orogenic wedge through time using changes to the active wedge width measured from the forward modeled cross section, and the relationship between propagation rate and shortening rate (Figure 12). The interaction between  $F_E$  and  $F_A$  is reflected in the ratio between thrust belt propagation and shortening rates; thus, we use this ratio as a proxy to interpret the self-similar shrinkage or growth of the wedge related to the mass flux balance (Figures 12b and 12c). At ratios greater than 1, forward propagation outpaces internal shortening, which reflects self-similar wedge growth to maintain critical taper (e.g.,  $F_A > F_E$ ). At ratios less than 1, forward propagation stalls as the wedge deforms internally, reflecting cessation of wedge growth or reduction in self-similar wedge size (e.g.,  $F_A < F_E$ ). At ratios close to one the wedge is at flux steady state and material is removed by erosion at approximately the same rate at which it is accreting ( $F_A = F_E$ ).

Following early shortening along the western margin of South America from ~100–45 Ma (e.g., DeCelles & Horton, 2003; Horton, 2018b; Sempere et al., 1997), the deformation front made a major eastward jump

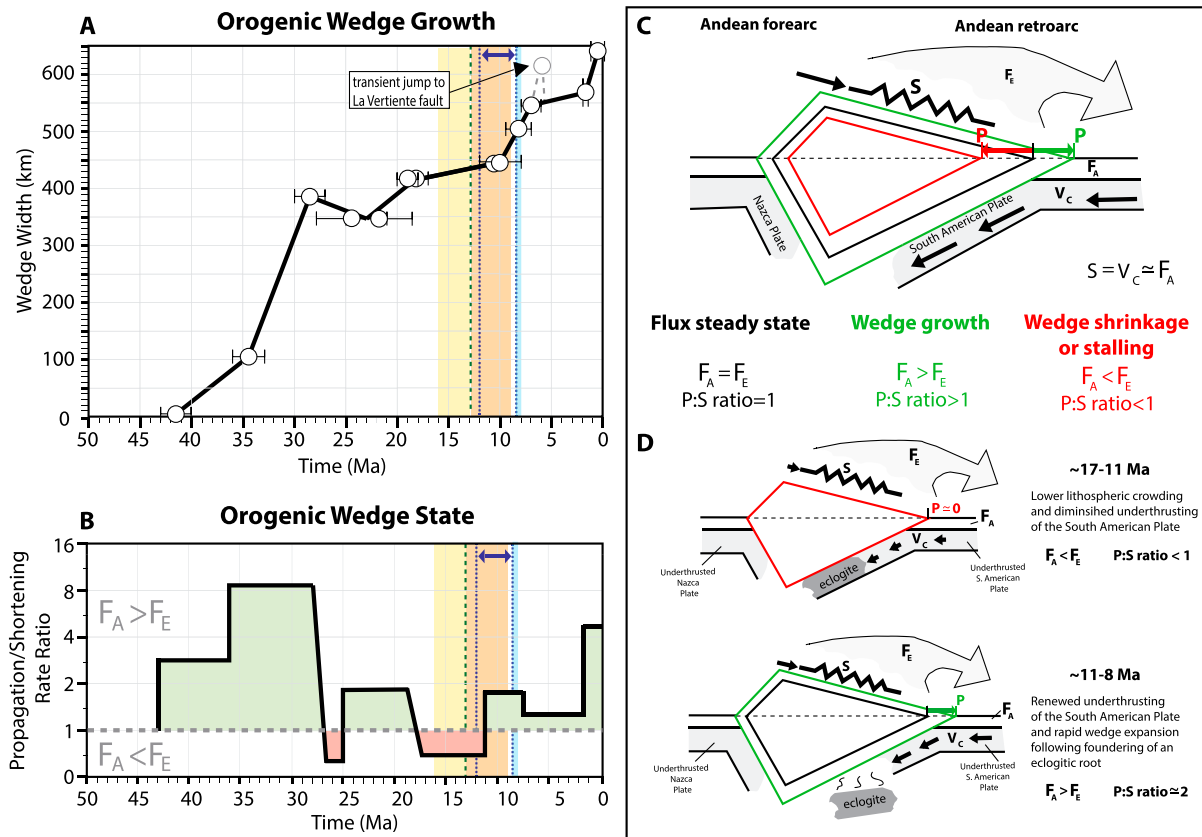


**Figure 12.** Orogenic wedge state through time at  $\sim 21^\circ\text{S}$ . (a) Width of the deformed wedge through time. A positive slope represents wedge expansion, and a negative slope represents wedge shrinkage. (b) Ratio of thrust front propagation rate and thrust belt shortening rate. A ratio less than 1 represents wedge shrinkage as accretionary influx ( $F_A$ ) < erosional efflux ( $F_E$ ), a ratio > 1 represents wedge expansion as  $F_A > F_E$ , and a ratio of  $\sim 1$  represents a steady state wedge ( $F_A = F_E$ ). Instantaneous changes in propagation/shortening rate ratios are an artifact of the limited time resolution in our shortening reconstructions (Figure 9), and gradual changes to the ratio are placed where there is uncertain overlap for deformation timing (e.g., 20–17 and 11–8 Ma; Figure 10b). (c) Schematic kinematic model of a critically tapered wedge (modified from DeCelles and DeCelles, 2001; Whipple, 2009). Green and red lines show self-similar wedge growth or shrinkage, and direction of propagation ( $P$ ) as erosional flux ( $F_E$ ) or accretionary influx into the wedge ( $F_A$ ) are modified from steady state.  $S$  is the horizontal shortening rate of the thrust belt, and  $V_c$  is the velocity of the underthrust foreland crust. (d) Schematic model of delamination, rapid underthrusting, and resulting rapid wedge propagation as  $F_A$  increases relative to  $F_E$ . Length of arrows is proportional to rate of  $V_c$ ,  $S$ , and  $P$ .

toward the continent interior (McQuarrie et al., 2005). At  $\sim 21^\circ\text{S}$ , the  $>500\text{-km}$  jump in the thrust front from the Western Cordillera into the EC by  $\sim 43\text{ Ma}$  (Figures 9a and 9b) was accomplished by emplacement of an  $\sim 11\text{--}12\text{ km}$  thick basement thrust sheet that fed slip eastward (Anderson et al., 2017) but resulted in a subcritical wedge (e.g., McQuarrie, 2002; McQuarrie et al., 2005). The basement thrust sheet fed slip into the overlying sedimentary cover via a décollement at the basement-cover interface (Figure 9). The impetus for this remarkable advance of the deformation front is unclear but could be explained by transmission of stresses due to (1) crustal rheology (strong Altiplano, weak EC), (2) reactivation of favorably oriented Paleozoic or Mesozoic structures, or (3) flat slab subduction (e.g., McQuarrie et al., 2005). However, geophysical data indicate that the rheology of the Altiplano crust is relatively weak compared to the EC (Beck & Zandt, 2002), which favors the latter two scenarios as probable explanations.

Between  $\sim 43$  and  $\sim 27\text{ Ma}$ , the active wedge width increased rapidly, achieving the highest ratios of propagation to shortening rate during the entire history of retroarc development (Figure 12). During initial wedge growth,  $F_E$  was less than the  $F_A$  because the total erosional area of the orogen was originally small, and the response time for a wedge to achieve flux steady state can be on the order of tens of million years depending on total rainfall and erodibility of the wedge material (Hilley et al., 2004). Initial wedge growth was accomplished by eastward wedging of the EC basement thrust sheet, and accompanying westward propagation of deformation through the EC cover sequence (Figures 9a–9c). The abrupt decrease in



sedimentary thickness at the EC-IAZ boundary may have acted as a rigid backstop that limited further eastward propagation of slip along the basement-cover décollement (e.g., Couzens-Schultz et al., 2003), favoring wedge growth by westward propagation of deformation in the sedimentary cover in the early stages of the thrust belt. After the thrust front propagated to the EC-Altiplano boundary at ~27 Ma, a phase of out-of-sequence shortening distributed across the EC (Figure 9d) resulted in a short-lived period of apparent wedge shrinkage (Figure 12a). However, overlapping age uncertainties during this period make it difficult to determine if actual wedge shrinkage occurred at this time, or if wedge growth was simply reduced to a much lower rate. Nevertheless, the response time for wedge growth to achieve a sufficient size for  $F_E$  to balance  $F_A$  and approach initial flux steady state occurs ~16–18 Myr after initiation of deformation at ~43 Ma (Figure 12b).

By ~25 Ma, the thrust belt had grown into a large enough wedge to promote eastward advance of deformation in the sedimentary cover toward the foreland (Figure 9d). Between ~25 and ~17 Ma, overall wedge width continued to increase, even as overall shortening nearly doubled (Figure 12a). This increase in wedge width can be attributed in part to a change to a weaker décollement, and hence, a lower critical taper angle, near the IAZ-EC boundary, where strong Cambrian quartzite at the basement-cover interface transitions eastward into weak Silurian shale (e.g., Kley, 1996). As a consequence of this reduced critical taper angle, the deformation front propagated rapidly eastward across the western IAZ. Shortening rates may have increased during this period due to structural imbrication of a much thinner sedimentary section in the IAZ, which would require higher shortening rates to maintain taper (e.g., Boyer, 1995). This is reflected in the development of a backthrust system, a higher shortening magnitude (~70%), and reduced thrust spacing in the western IAZ (Anderson et al., 2017).

Between ~17 and ~11 Ma, wedge expansion slowed considerably, growing from a width of ~410 to only ~450 km as the propagation/shortening rate ratio decreased to <1 (Figures 12a and 12b). The deformation front stalled in the central IAZ, shortening rates decreased, and out-of-sequence deformation was distributed across the hinterland (Figure 9e). The majority of shortening was focused in the Altiplano, with minor shortening in the Tupiza region in the western EC. This timeframe is also consistent with slowing of thrust belt growth in central and northern Bolivia (Barnes et al., 2006, 2008; McQuarrie, Barnes, & Ehlers, 2008). We suggest that negative buoyancy and crowding of the lower lithosphere associated with the buildup of a dense eclogitic root (e.g., DeCelles et al., 2009) could explain this decrease in shortening rates, the focusing of deformation in the Altiplano, and stagnation of the eastward migration of the thrust front (Figure 12d). Prior to ~16–13 Ma, the southern Altiplano and EC were apparently at low elevation, possibly <1 km (Cadena et al., 2015; Garzione et al., 2014; Gregory-Wodzicki et al., 1998), despite ~65% of the total shortening of the retroarc thrust belt being accomplished by this time (Figure 10a). This shortening should have resulted in isostatic surface uplift due to crustal thickening (e.g., Hoke et al., 2007; Lamb, 2015). However, growth of an eclogitic root beneath the arc and hinterland may have induced a regional isostatic depression of surface elevation that resulted in stalling of the deformation front by promoting increased internal shortening (DeCelles et al., 2009, 2015; Garzione et al., 2006). Accordingly, mass balance calculations derived from shortening estimates indicate that the crustal thicknesses required to generate eclogitic phases from mafic lower crust ( $\geq 50$  km; e.g., Kay & Kay, 1993) below the southern Altiplano-EC may have been achieved before ~20 Ma (Anderson et al., 2017; Eichelberger et al., 2015), and geochemical and isotopic data from lavas in southern Bolivia suggest that a dense root was present below the Altiplano between ~16–11 Ma (Kay & Coira, 2009). Additionally, crowding of the lithosphere may have impeded westward underthrusting beneath the orogen (DeCelles et al., 2009; McQuarrie et al., 2005), which could perturb the flux balance of the wedge by reducing thrust belt shortening rates, and thereby rates of frontal accretion. If  $F_E$  remained the same as  $F_A$  was reduced, then the wedge should have responded with a slowing or cessation of propagation, with out-of-sequence deformation focused in the wedge interior to maintain taper (e.g., Whipple & Meade, 2006).

### 7.3. Orogenic Wedge Response After Middle Miocene Rapid Surface Uplift of the Hinterland

After ~11 Ma, the wedge width expanded rapidly from ~450 km to the present-day width of ~640 km (Figure 12a). However, the propagation/shortening rate ratio was variable over this time period, increasing initially at 11 Ma, and then primarily decreasing until ~1.5 Ma (Figure 12b). From ~11 to 8 Ma, a return to high eastward propagation rates (~27 mm/year) was accompanied by relatively high shortening rates (~15 mm/year), resulting in a propagation/shortening rate ratio that was only slightly less than 2. Wedge growth was

renewed by rapid eastward propagation of the thrust front from the central IAZ to the IAZ-SAZ boundary, and cessation of shortening in the EC-Altiplano (Figures 9e and 9f).

Stable isotope and paleobotanical paleoaltimetry data from southern Bolivia suggest  $2.5 \pm 1.0$  km of surface uplift for the Altiplano and EC between 16 and 13 Ma, and an additional  $0.7 \pm 0.6$  km between 13 and 9 Ma (Garzione et al., 2014; Gregory-Wodzicki et al., 1998). This is corroborated by giant tortoise and freshwater chelid fossil discoveries in the Que Brada Honda that suggest that the EC was at an elevation  $<1$  km prior to  $\sim 13$  Ma (Cadena et al., 2015), which narrows the time frame for surface uplift to  $\sim 13$ –9 Ma. Delamination of dense eclogitic lower crust and mantle lithosphere has been called upon as a mechanism to explain the absence of mafic lower crust in the hinterland of the central Andes (Beck & Zandt, 2002; Kay & Coira, 2009; Ryan et al., 2016), as well as the trigger for rapid Miocene surface uplift events in the EC and Altiplano (Garzione et al., 2006, 2008, 2014; Molnar & Garzione, 2007), and is a key prediction of the Cordilleran cyclicity model (DeCelles et al., 2009, 2015).

The rapid eastward propagation of the wedge that we document starting at  $\sim 11$ –8 Ma closely corresponds with the timing of surface uplift in the EC-Altiplano, particularly if the majority of uplift occurred after  $\sim 13$  Ma (e.g., Cadena et al., 2015), which suggests that the two processes are linked by a cause-and-effect relationship. Rapid surface uplift can drive wedge expansion if the increase in surface slope is great enough for the gravitational potential of the system to overcome the basal frictional resistance to sliding (Dahlen, 1984; Garzione et al., 2006). Additionally, the foundering of an eclogitic root creates space for increased underthrusting (Figure 12d; Currie et al., 2015; DeCelles et al., 2009, 2015), which should result in an increase in  $F_A$  and rapid wedge growth in order to maintain critical taper (e.g., Whipple & Meade, 2006).

The middle Miocene increase in surface topography and uplift of the hinterland plateau altered the climate of the central Andes (Ehlers & Poulsen, 2009). Pedogenic carbonates in the SAZ ( $\sim 21$ – $22^\circ$ S) record a  $\sim 5\%$  decrease in  $\delta^{18}\text{O}$  values between  $\sim 12$  and 8.5 Ma that are interpreted as an increase in rainout and precipitation in response to the growing topography of the EC, followed by a  $\sim 3\%$  increase in  $\delta^{18}\text{O}$  at  $\sim 8.5$  Ma that reflects increasing seasonality of rainfall (Mulch et al., 2010). As wedge width and surface elevation increases, erosion should gradually occur over a wider area, allowing  $F_E$  to eventually come back into balance with  $F_A$  after some response time, which is predicted to slow the propagation rate of the thrust front (Whipple & Meade, 2006). Consistent with increasing precipitation rates interpreted between  $\sim 12$  and 8.5 Ma, rapid outward expansion of the wedge slowed and forward propagation rates began to decrease by  $\sim 8$  Ma (Figure 10b). From  $\sim 8$  to 1.5 Ma, the forward propagation rate decreased to the point that the propagation/shortening rate ratio approached a steady state value closer to  $\sim 1$  (Figure 12b). The positive  $\delta^{18}\text{O}$  increase in pedogenic carbonates is indicative of a further climatic shift to more seasonal precipitation between  $\sim 9$  and 8 Ma (Mulch et al., 2010) and likely occurred in response to the generation of an orographic barrier as the EC-Altiplano attained critical elevations  $>3$  km (Ehlers & Poulsen, 2009). A shift to more seasonal precipitation and southward deflection of the South American low-level jet resulted in focused precipitation and increased erosional efficiency along the eastern flank of the mountain belt, as reflected in the fourfold increase in sedimentation rates in the Chaco foreland basin between  $\sim 8$  and 6 Ma (Bookhagen & Strecker, 2008; Mulch et al., 2010; Strecker et al., 2007; Uba et al., 2009). Thus, changing climate conditions in response to growing topography are interpreted to have slowed propagation rates by increasing erosional efficiency and enhancing removal of material from the eastern flank of the thrust belt, which promoted steady state conditions. The wedge attained an approximately full steady state for  $\sim 6.5$  Myr whereby erosional removal kept pace with material accretion, and shortening rates matched propagation rates, until  $\sim 1.5$  Ma (Figures 11 and 12).

After  $\sim 1.5$  Ma, the propagation/shortening rate ratio increased to  $>4$ , indicating a significant increase in wedge growth rate (Figure 12a). It is unclear what drove this rapid thrust front advance, though weakening of the basal décollement by increasing pore fluid pressure (e.g., Uba et al., 2009) or strain weakening (e.g., Oncken et al., 2012) could be likely explanations. However, outward expansion of the orographic barrier may have reduced the area over which effective erosion occurred on the flank of the wedge. The ensuing increased aridification and reduced hinterland erosion (Sobel et al., 2003; Sobel & Strecker, 2003; Strecker et al., 2007) could have led to significantly lower erosional flux relative to accretionary influx within the hinterland, promoting rapid self-similar wedge growth to maintain flux steady-state.

Alternatively, the most recent period of deformation is a short-term transient phase, and similar phases could have occurred during long-term wedge evolution, but the geological record may have insufficient resolution to capture such perturbations.

## 8. Conclusions

1. Deformation initiated in the EC at ~43 Ma and propagated westward to the EC-Altiplano boundary by ~27 Ma. After ~27 Ma, deformation was distributed across the EC and Altiplano. Eastward advance into the western and eastern portions of the IAZ occurred from ~25 to 17 Ma and ~11 to 8 Ma, respectively. In the intervening period, out-of-sequence shortening was focused in the EC and Altiplano. SAZ deformation began at ~8–7 Ma and progressed eastward to the active thrust front in the Chaco Plain.
2. The thrust belt grew self-similarly first by westward propagation of deformation in the sedimentary cover as the upper basement thrust sheet was wedged eastward between ~43 and ~25 Ma but switched to eastward advance into the IAZ between ~25 and ~17 Ma. We attribute this switch to a reduction in decollement strength, which reduced the critical taper angle and promoted rapid eastward propagation through the sedimentary cover. Stalling of the deformation front in the central IAZ from ~17 to 11 Ma corresponded to slowed accretionary influx, which we interpret to be related to lithospheric crowding. Rapid hinterland surface uplift at ~13–9 Ma is attributed to eclogite removal and resulted in increased accretionary influx and resumed rapid propagation across the eastern IAZ at ~11 Ma. Continued wedge expansion after ~9 Ma, and additional surface uplift, is attributed to increased accretionary influx facilitated by eclogite removal. Wedge growth was counteracted by development of an orographic barrier that induced a climatic shift at ~8.5 Ma, which enhanced erosional efficiency along the eastern flank of the orogen, slowing propagation until ~1.5 Ma.
3. Our records appear to validate key predictions of the Cordilleran cyclicity model, where changes in surface topography are related to the buildup and foundering of eclogite, which in turn affects the propagation of the thrust front by perturbing the balance of mass flux into the orogen.

## Acknowledgments

This work was funded by National Science Foundation grant EAR-1250510 awarded to Long and Horton. Additional funds for analyses were provided by Repsol Bolivia S.A. Nathan Eichelberger and Richard Lease are thanked for constructive reviews that improved this manuscript. We thank Ramiro Matos for assistance with logistics, and Javier Matos for driving, translating, logistics, and assistance in the field. Laboratory analyses and data interpretation at UT Austin were aided by discussions and assistance from Nick Perez, Margo Oldum, Doug Barber, Sol Cooperdock, Emily Cooperdock, Mike Prior, Renas Kroshnaw, and Tomas Capaldi. We thank Harald Ege and Ed Sobel for sharing individual grain ages from their published AFT ages. The data presented in this manuscript can be found in the supporting information.

## References

- Allmendinger, R. W., Jordan, T. E., Kay, S. M., & Isacks, B. L. (1997). Altiplano-Puna Plateau of the Central Andes. *Annual Review of Earth and Planetary Sciences*, 25(1), 139–174. <https://doi.org/10.1146/annurev.earth.25.1.139>
- Allmendinger, R. W., Ramos, V. A., Jordan, T. E., Palma, M., & Isacks, B. (1983). Paleogeography and Andean structural geometry, north-west Argentina. *Tectonics*, 2(1), 1–16. <https://doi.org/10.1029/TC002i001p00001>
- Allmendinger, R. W., & Zapata, T. R. (2000). The footwall ramp of the Subandean decollement, northernmost Argentina, from extended correlation of seismic reflection data. *Tectonophysics*, 321(1), 37–55. [https://doi.org/10.1016/S0040-1951\(00\)00077-9](https://doi.org/10.1016/S0040-1951(00)00077-9)
- Anderson, R. B., Long, S. P., Horton, B. K., Calle, A. Z., & Ramirez, V. (2017). Shortening and structural architecture of the Andean fold-thrust belt of southern Bolivia (21°S): Implications for kinematic development and crustal thickening of the central Andes. *Geosphere*, 13. <https://doi.org/10.1130/GES01433.1>
- Armstrong, P. a. (2005). Thermochronometers in sedimentary basins. *Reviews in Mineralogy and Geochemistry*, 58(1), 499–525. <https://doi.org/10.2138/rmg.2005.58.19>
- Arriagada, C., Cobbold, P. R., & Roperch, P. (2006). Salar de Atacama basin: A record of compressional tectonics in the Central Andes since the mid-Cretaceous. *Tectonics*, 25, TC1008. <https://doi.org/10.1029/2004TC001770>
- Arriagada, C., Roperch, P., Mpodozis, C., & Cobbold, P. R. (2008). Paleogene building of the Bolivian Orocline: Tectonic restoration of the central Andes in 2-D map view. *Tectonics*, 27, TC6014. <https://doi.org/10.1029/2008TC002269>
- Baby, P., Hérail, G., Salinas, R., & Sempere, T. (1992). Geometry and kinematic evolution of passive roof duplexes deduced from cross section balancing: Example from the foreland thrust system of the southern Bolivian Subandean. *Tectonics*, 11, 523–536.
- Barnes, J. B., & Ehlers, T. A. (2009). End member models for Andean plateau uplift. *Earth-Science Reviews*, 97(1–4), 105–132. <https://doi.org/10.1016/j.earscirev.2009.08.003>
- Barnes, J. B., Ehlers, T. A., McQuarrie, N., O'Sullivan, P. B., & Pelletier, J. D. (2006). Eocene to recent variations in erosion across the central Andean fold-thrust belt, northern Bolivia: Implications for plateau evolution. *Earth and Planetary Science Letters*, 248(1–2), 118–133. <https://doi.org/10.1016/j.epsl.2006.05.018>
- Barnes, J. B., Ehlers, T. A., McQuarrie, N., O'Sullivan, P. B., & Tawackoli, S. (2008). Thermochronometer record of central Andean Plateau growth, Bolivia (19.5°S). *Tectonics*, 27, TC3003. <https://doi.org/10.1029/2007TC002174>
- Barnes, J. B., Ehlers, T. A., Insel, N., McQuarrie, N., & Poulsen, C. J. (2012). Linking orography, climate, and exhumation across the central Andes. *Geology*, 40(12), 1135–1138. <https://doi.org/10.1130/G33229.1>
- Bascañán, S., Arriagada, C., Le Roux, J., & Deckart, K. (2016). Unraveling the Peruvian phase of the Central Andes: Stratigraphy, sedimentology and geochronology of the Salar de Atacama Basin (22°30'–23°S), northern Chile. *Basin Research*, 28, 365–392.
- Beck, S. L., & Zandt, G. (2002). The nature of orogenic crust in the central Andes. *Journal of Geophysical Research*, 107(B10), 2230. <https://doi.org/10.1029/2000JB000124>
- Bernet, M. (2009). A field-based estimate of the zircon fission-track closure temperature. *Chemical Geology*, 259(3–4), 181–189. <https://doi.org/10.1016/j.chemgeo.2008.10.043>
- Bookhagen, B., & Strecker, M. R. (2008). Orographic barriers, high-resolution TRMM rainfall relief variations along the eastern Andes. *Geophysical Research Letters*, 35, L06403. <https://doi.org/10.1029/2007GL032011>

- Boyer, S. (1995). Sedimentary basin taper as a factor controlling the geometry and advance of thrust belts. *American Journal of Science*, 295(10), 1220–1254. <https://doi.org/10.2475/ajs.295.10.1220>
- Brandon, K. A., Roden-Tice, T. M., & Garver, J. I. (1998). Late Caneozoic exhumation of the cascadia accretionary wedge in the Olympic mountains, northwest Washington State. *Geological Society of America Bulletin*, 110(8), 985–1009. [https://doi.org/10.1130/0016-7606\(1998\)110<0985:LCEOTC>2.3.CO;2](https://doi.org/10.1130/0016-7606(1998)110<0985:LCEOTC>2.3.CO;2)
- Brooks, B. a., Bevis, M., Whipple, K., Ramon Arrowsmith, J., Foster, J., Zapata, T., et al. (2011). Orogenic-wedge deformation and potential for great earthquakes in the central Andean backarc. *Nature Geoscience*, 4(6), 380–383. <https://doi.org/10.1038/ngeo1143>
- Buiter, S. (2012). A review of brittle compressional wedge models. *Tectonophysics*, 530–531, 1–17. <https://doi.org/10.1016/j.tecto.2011.12.018>
- Cadena, E. A., Anaya, F., & Croft, D. A. (2015). Giant fossil tortoise and freshwater chelid turtle remains from the middle Miocene, Quebrada Honda, Bolivia: Evidence for lower paleoelevations for the southern Altiplano. *Journal of South American Earth Sciences*, 64, 190–198. <https://doi.org/10.1016/j.jsames.2015.10.013>
- Calte, A. Z. (2013). Neogene sedimentation and provenance record of the Subandean Zone and Chaco foreland basin, southern Bolivia, Master's thesis, University of Texas at Austin, Austin, Texas, 138 p.
- Calte, A. Z., Horton, B. K., Limachi, R., Stockli, D. F., Uzeda-Orellana, G. V., Anderson, R. B., & Long, S. P. (2018). Cenozoic provenance and depositional record of the Subandean foreland basin during growth and advance of the central Andean fold-thrust belt, southern Bolivia. In G. Zamora, K. McClay, & V. Ramos (Eds.), *Petroleum basins and hydrocarbon potential of the Andes of Peru and Bolivia*, American Association of Geologists Memoir (Vol. 117, chapter 18, pp. 459–506). <https://doi.org/10.1306/13622132m1173777>
- Cardozo, N., & Jordan, T. (2001). Causes of spatially variable tectonic subsidence in the Miocene Bermejo Foreland Basin, Argentina. *Basin Research*, 13(3), 335–357. <https://doi.org/10.1046/j.0950-091X.2001.00154.x>
- Carrapa, B., & DeCelles, P. G. (2015). Regional exhumation and kinematic history of the central Andes in response to cyclical orogenic processes. In Memoir of the Geological Society of America (Vol. 212, Chapter 11, pp. 201–213). (Memoir of the Geological Society of America; Vol. 212). Geological Society of America. [https://doi.org/10.1130/2015.1212\(11\)](https://doi.org/10.1130/2015.1212(11))
- Coney, P. J., & Evenchick, C. a. (1994). Consolidation of the American Cordilleras. *Journal of South American Earth Sciences*, 7(3–4), 241–262. [https://doi.org/10.1016/0895-9811\(94\)90011-6](https://doi.org/10.1016/0895-9811(94)90011-6)
- Costa, C. H., Audemard, F. A. M., Bezerra, F. H. R., Lavenue, A., Machette, M. N., & Paris, G. (2006). An overview of the main Quaternary deformation of South America. *Revista de la Asociación Geológica Argentina*, 61, 461–479.
- Couzens-Schultz, B. A., Vendeville, B. C., & Wiltchko, D. V. (2003). Duplex style and triangle zone formation: Insights from physical modeling. *Journal of Structural Geology*, 10, 1623–1644. [https://doi.org/10.1016/S0191-8141\(03\)00004-X](https://doi.org/10.1016/S0191-8141(03)00004-X)
- Currie, C. A., Ducea, M. N., DeCelles, P. G., & Beaumont, C. (2015). Geodynamic models of Cordilleran orogens: Gravitational instability of magmatic arc roots. In Memoir of the Geological Society of America (Vol. 212, ch. 1, pp. 1–22). (Memoir of the Geological Society of America; Vol. 212). Geological Society of America. [https://doi.org/10.1130/2015.1212\(01\)](https://doi.org/10.1130/2015.1212(01))
- Dahlen, F. A. (1984). Noncohesive critical Coulomb wedges: An exact solution. *Journal of Geophysical Research*, 89, 10,125–10,133.
- Dahlen, F. A. (1990). Critical taper model of fold-and-thrust belts and accretionary wedges. *Annual Review of Earth and Planetary Sciences*, 18(1), 55–99. <https://doi.org/10.1146/annurev.ea.18.050190.000415>
- Dahlen, F. A., & Suppe, J. (1988). Mechanics, growth, and erosion of mountain belts. *Special Papers: Geological Society of America*, 218, 161–178.
- Davis, D., Suppe, J., & Dahlen, F. A. (1983). Mechanics of fold-and-thrust belts and accretionary wedges. *Journal of Geophysical Research*, 88(B2), 1153–1172. <https://doi.org/10.1029/JB088iB02p01153>
- DeCelles, P. G., & DeCelles, P. C. (2001). Rates of shortening, propagation, underthrusting, and flexural wave migration in continental orogenic systems. *Geology*, 29, 135–138. [https://doi.org/10.1130/0091-7613\(2001\)029<0135:ROSPUA>2.0.CO;2](https://doi.org/10.1130/0091-7613(2001)029<0135:ROSPUA>2.0.CO;2)
- DeCelles, P. G., Ducea, M. N., Kapp, P., & Zandt, G. (2009). Cyclicity in Cordilleran orogenic systems. *Nature Geoscience*, 2(4), 251–257. <https://doi.org/10.1038/ngeo469>
- DeCelles, P. G., & Graham, S. A. (2015). Cyclical processes in the North American Cordilleran orogenic system. *Geology*, 43(6), 499–502. <https://doi.org/10.1130/G36482.1>
- DeCelles, P. G., & Horton, B. K. (2003). Early to middle Tertiary foreland basin development and the history of Andean crustal shortening in Bolivia. *Geological Society of America Bulletin*, 115(1), 58–77. [https://doi.org/10.1130/0016-7606\(2003\)115<0058:ETMTFB>2.0.CO;2](https://doi.org/10.1130/0016-7606(2003)115<0058:ETMTFB>2.0.CO;2)
- DeCelles, P. G., & Mitra, G. (1995). History of the Sevier orogenic wedge in terms of critical taper models, northeast Utah and southwest Wyoming. *Geological Society of America Bulletin*, 107(4), 454–462. [https://doi.org/10.1130/0016-7606\(1995\)107<0454:HOTSOW>2.3.CO;2](https://doi.org/10.1130/0016-7606(1995)107<0454:HOTSOW>2.3.CO;2)
- DeCelles, P. G., Zandt, G., Beck, S. L., Currie, C. A., Ducea, M. N., Kapp, P., et al. (2015). Cyclical orogenic processes in the Cenozoic central Andes. In P. G. DeCelles, M. N. Ducea, B. Carrapa, & P. A. Kapp (Eds.), *Geodynamics of a Cordilleran orogenic system: The central Andes of Argentina and Northern Chile*, Geological Society of America Memoirs (Vol. 212, pp. 459–490). [https://doi.org/10.1130/2015.1212\(22\)](https://doi.org/10.1130/2015.1212(22))
- Dewey, J. F., & Bird, J. M. (1970). Mountain belts and the new global tectonics. *Journal of Geophysical Research*, 75(14), 2625–2647. <https://doi.org/10.1029/JB075i014p02625>
- Dodson, M. H. (1973). Closure temperatures in cooling geological and petrological systems. *Contributions to Mineralogy and Petrology*, 40, 259–274.
- Donelick, R. A., O'Sullivan, P. B., & Ketchum, R. A. (2005). Apatite fission-track analysis. *Reviews in Mineralogy and Geochemistry*, 58, 49–94. <https://doi.org/10.2138/rmg.2005.58.3>
- Ducea, M. N. (2002). Constraints on the bulk composition and root foundering rates of continental arcs: A California arc perspective. *Journal of Geophysical Research*, 107(B11), 2304. <https://doi.org/10.1029/2001JB000643>
- Ducea, M. N., Otamendi, J. E., Bergantz, G. W., Jianu, D., & Petrescu, L. (2015). The origin and petrologic evolution of the Ordovician Famatinian-Puna arc. In Memoir of the Geological Society of America (Vol. 212, ch. 7, pp. 125–138). (Memoir of the Geological Society of America; Vol. 212). Geological Society of America. [https://doi.org/10.1130/2015.1212\(07\)](https://doi.org/10.1130/2015.1212(07))
- Ducea, M. N., Seclaman, A. C., Murray, K. E., Jianu, D., & Schoenbohm, L. M. (2013). Mantle-drip magmatism beneath the Altiplano-Puna Plateau, cen- tral Andes. *Geology*, 41(8), 915–918. <https://doi.org/10.1130/G34509.1>
- Dunn, J., Hartshorn, K., & Hartshorn, P. (1995). Structural styles and hydrocarbon potential of the Sub-Andean thrust belt of southern Bolivia. In A. J. Tankard, R. Suarez Soruco, & H. J. Welsink (Eds.), *Petroleum basins of South America*, AAPG Memoir (Vol. 62, pp. 523–543).
- Echavarría, L., Hernández, R., Allmendinger, R., & Reynolds, J. (2003). Subandean thrust and fold belt of northwestern Argentina: Geometry and timing of the Andean evolution. *American Association of Petroleum Geologists Bulletin*, 87(6), 965–985. <https://doi.org/10.1306/01200300196>
- Ege, H. (2004). Exhumations-und Hebungsgeschichte der zentralen Anden in Südbolivien (2185) durch Spaltspur-Thermochronologie an Apatit. PhD thesis, Freie Universität Berlin, Berlin. 159 pp.



- Ege, H., Sobel, E. R., Scheuber, E., & Jacobshagen, V. (2007). Exhumation history of the southern Altiplano plateau (southern Bolivia) constrained by apatite fission track thermochronology. *Tectonics*, 26, TC1004. <https://doi.org/10.1029/2005TC001869>
- Egenhoff, S. O., Maletz, J., Weber, B., & Erdtmann, B.-D. (2002). The middle Ordovician Jurcumá section: A pinpoint for the evolution of southern Bolivia. *Freiberger Forschungshefte*, C497, 9–17.
- Ehlers, T. A. (2005). Crustal thermal processes and the interpretation of thermochronometric data. *Reviews in Mineralogy and Geochemistry*, 58(1), 315–350. <https://doi.org/10.2138/rmg.2005.58.12>
- Ehlers, T. A., & Poulsen, C. J. (2009). Influence of Andean uplift on climate and paleoaltimetry estimates. *Earth and Planetary Science Letters*, 281(3–4), 238–248. <https://doi.org/10.1016/j.epsl.2009.02.026>
- Eichelberger, N., & McQuarrie, N. (2015). Kinematic reconstruction of the Bolivian orocline. *Geosphere*, 11(2), 445–462. <https://doi.org/10.1130/GES01064.1>
- Eichelberger, N., McQuarrie, N., Ehlers, T. A., Enkelmann, E., Barnes, J. B., & Lease, R. O. (2013). New constraints on the chronology, magnitude, and distribution of deformation within the central Andean orocline. *Tectonics*, 32, 1432–1453. <https://doi.org/10.1002/tect.20073>
- Eichelberger, N., McQuarrie, N., Ryan, J., Karimi, B., Beck, S., & Zandt, G. (2015). Evolution of crustal thickening in the central Andes, Bolivia. *Earth and Planetary Science Letters*, 426, 191–203. <https://doi.org/10.1016/j.epsl.2015.06.035>
- Elger, K., Oncken, O., & Glodny, J. (2005). Plateau-style accumulation of deformation: Southern Altiplano. *Tectonics*, 24, TC4020. <https://doi.org/10.1029/2004TC001675>
- Enkelmann, E., Valla, P. G., & Champagnac, J. D. (2015). Low-temperature thermochronology of the Yakutat plate corner, St. Elias Range (Alaska): Bridging short-term and long-term deformation. *Quaternary Science Reviews*, 113, 23–38. <https://doi.org/10.1016/j.quascirev.2014.10.019>
- Farley, K. A. (2000). Helium diffusion from apatite: General behavior as illustrated by Durango fluorapatite. *Journal of Geophysical Research*, 105, 2903. <https://doi.org/10.1029/1999JB900348>
- Farley, K. A. (2002). (U-Th)/He dating: Techniques, calibrations, and applications. *Reviews in Mineralogy and Geochemistry*, 47(1), 819–844. <https://doi.org/10.2138/rmg.2002.47.18>
- Flowers, R. M., Ketcham, R. A., Shuster, D. L., & Farley, K. A. (2009). Apatite (U-Th)/He thermochronometry using a radiation damage accumulation and annealing model. *Geochimica et Cosmochimica Acta*, 73(8), 2347–2365. <https://doi.org/10.1016/j.gca.2009.01.015>
- Galbraith, R. (2005). *Statistics for fission track analysis*, (p. 240). Boca Raton, FL: Chapman & Hall/CRC. <https://doi.org/10.1201/9781420034929>
- Galbraith, R. F. (1981). On statistical models for fission track counts. *Journal of the International Association for Mathematical Geology*, 13(6), 471–478. <https://doi.org/10.1007/BF01034498>
- Gallagher, K., Brown, R., & Johnson, C. (1998). Fission track analysis and its applications to geological problems. *Annual Review of Earth and Planetary Sciences*, 26(1), 519–572. <https://doi.org/10.1146/annurev.earth.26.1.519>
- Garzione, C. N., Auerbach, D., Smith, J. J., Rosario, J., Passey, B. H., Jordan, T. E., & Eiler, J. M. (2014). Clumped isotope evidence for diachronous surface cooling of the Altiplano and pulsed surface uplift of the Central Andes. *Earth and Planetary Science Letters*, 393, 173–181. <https://doi.org/10.1016/j.epsl.2014.02.029>
- Garzione, C. N., Hoke, G. D., Libarkin, J. C., Withers, S., MacFadden, B., Eiler, J., et al. (2008). Rise of the Andes. *Science*, 320(5881), 1304–1307. <https://doi.org/10.1126/science.1148615>
- Garzione, C. N., McQuarrie, N., Perez, N. D., Ehlers, T. A., Beck, S. L., Kar, N., et al. (2017). The tectonic evolution of the central Andean plateau and geodynamic implications for the growth of plateaus. *Annual Review of Earth and Planetary Sciences*, 45(1), 529–559. <https://doi.org/10.1146/annurev-earth-063016-020612>
- Garzione, C. N., Molnar, P., Libarkin, J., & MacFadden, B. (2006). Rapid late Miocene rise of the Bolivian Altiplano: Evidence for removal of mantle lithosphere. *Earth and Planetary Science Letters*, 241(3–4), 543–556. <https://doi.org/10.1016/j.epsl.2005.11.026>
- Gillis, R. J., Horton, B. K., & Grove, M. (2006). Thermochronology, geochronology, and upper crustal structure of the Cordillera Real: Implications for Cenozoic exhumation of the central Andean plateau. *Tectonics*, 25, TC6007. <https://doi.org/10.1029/2005TC001887>
- Gleadow, A. J. W., & Duddy, I. R. (1981). A natural long term annealing experiment for apatite. *Nuclear Tracks*, 5(1–2), 169–174. [https://doi.org/10.1016/0191-278X\(81\)90039-1](https://doi.org/10.1016/0191-278X(81)90039-1)
- Gleadow, A. J. W., Duddy, I. R., Green, P. F., & Lovering, J. F. (1986). Confined fission track lengths in apatite: A diagnostic tool for thermal history analysis. *Contributions to Mineralogy and Petrology*, 94, 405–415.
- Green, P. F. (1981). A new look at statistics in fission-track dating. *Nuclear Tracks*, 5(1–2), 77–86. [https://doi.org/10.1016/0191-278X\(81\)90029-9](https://doi.org/10.1016/0191-278X(81)90029-9)
- Green, P. F., Duddy, I. R., Gleadow, A. J. W., Tingate, P. R., & Laslett, G. M. (1986). Thermal annealing of fission tracks in apatite 1. Variable temperature behaviour. *Chemical Geology: Isotope Geoscience Section*, 73(1), 25–38. [https://doi.org/10.1016/0168-9622\(88\)90019-X](https://doi.org/10.1016/0168-9622(88)90019-X)
- Gregory-Wodzicki, K. M., McIntosh, W. C., & Velasquez, K. (1998). Climatic and tectonic implications of the late Miocene Jakokkota flora, Bolivian Altiplano. *Journal of South American Earth Sciences*, 11, 533–560.
- Gubbels, T., Isacks, B., & Farrar, E. (1993). High-level surfaces, plateau uplift, and foreland development, Bolivian central Andes. *Geology*, 21, 695–698.
- Guenther, W. R., Reiners, P. W., Ketcham, R. A., Nasdala, L., & Giester, G. (2013). Helium diffusion in natural zircon: Radiation damage, anisotropy, and the interpretation of zircon (U-Th)/He thermochronology. *American Journal of Science*, 313, 145–198. <https://doi.org/10.2475/03.2013.01>
- Henry, S. G., & Pollack, H. N. (1988). Terrestrial heat flow above the Andean subduction zone in Bolivia and Peru. *Journal of Geophysical Research*, 93(B12), 15,153–15,162. <https://doi.org/10.1029/JB093iB12p15153>
- Hérail, G., Oller, J., Baby, P., Bonhomme, M., & Soler, P. (1996). Strike-slip faulting, thrusting and related basins in the Cenozoic evolution of the southern branch of the Bolivian Orocline. *Tectonophysics*, 259(1–3), 201–212. [https://doi.org/10.1016/0040-1951\(95\)00108-5](https://doi.org/10.1016/0040-1951(95)00108-5)
- Hilley, G., Strecker, M., & Ramos, V. (2004). Growth and erosion of fold-and-thrust belts with an application to the Aconcagua fold-and-thrust belt, Argentina. *Journal of Geophysical Research*, 109, B01410. <https://doi.org/10.1029/2002JB002282>
- Hoke, G. D., & Garzione, C. N. (2008). Paleosurfaces, paleoelevation, and the mechanisms for the late Miocene topographic development of the Altiplano plateau. *Earth and Planetary Science Letters*, 271(1–4), 192–201. <https://doi.org/10.1016/j.epsl.2008.04.008>
- Hoke, G. D., Isacks, B. L., Jordan, T. E., Blanco, N., Tomlinson, A. J., & Ramezani, J. (2007). Geomorphic evidence for post-10 Ma uplift of the western flank of the central Andes 18°30'–22°S. *Tectonics*, 26, TC5021. <https://doi.org/10.1029/2006TC002082>
- Horton, B. K. (1998). Sediment accumulation on top of the Andean orogenic wedge: Oligocene to late Miocene basins of the Eastern Cordillera, southern Bolivia. *Geological Society of America Bulletin*, 110(9), 1174–1192. [https://doi.org/10.1130/0016-7606\(1998\)110<1174:SAOTOT>2.3.CO;2](https://doi.org/10.1130/0016-7606(1998)110<1174:SAOTOT>2.3.CO;2)
- Horton, B. K. (1999). Erosional control on the geometry and kinematics of thrust belt development in the central Andes. *Tectonics*, 18(6), 1292–1304. <https://doi.org/10.1029/1999TC900051>



- Horton, B. K. (2005). Revised deformation history of the central Andes: Inferences from Cenozoic foredeep and intermontane basins of the Eastern Cordillera, Bolivia. *Tectonics*, 24, TC3011. <https://doi.org/10.1029/2003TC001619>
- Horton, B. K. (2018a). Tectonic regimes of the central and southern Andes: Responses to variations in plate coupling during subduction. *Tectonics*, 37, 402–429. <https://doi.org/10.1002/2017TC004624>
- Horton, B. K. (2018b). Sedimentary record of Andean mountain building. *Earth-Science Reviews*, 178, 279–309. <https://doi.org/10.1016/j.earscirev.2017.11.025>
- Horton, B. K., & DeCelles, P. G. (1997). The modern foreland basin system adjacent to the Central Andes. *Geology*, 25(10), 895–898. [https://doi.org/10.1130/0091-7613\(1997\)025<0895:TMFBSA>2.3.CO;2](https://doi.org/10.1130/0091-7613(1997)025<0895:TMFBSA>2.3.CO;2)
- Horton, B. K., Hampton, B. A., & Wanders, G. L. (2001). Paleogene synorogenic sedimentation in the Altiplano plateau and implications for initial mountain building in the central Andes. *Geological Society of America Bulletin*, 113(11), 1387–1400. [https://doi.org/10.1130/0016-7606\(2001\)113<1387:PSSITA>2.0.CO;2](https://doi.org/10.1130/0016-7606(2001)113<1387:PSSITA>2.0.CO;2)
- Hulka, C. (2005). Sedimentary and tectonic evolution of the Cenozoic Chaco foreland basin, Southern Bolivia. PhD Thesis, Freie Universität Berlin.
- Husson, L., & Sempere, T. (2003). Thickening the Altiplano crust by gravity-driven crustal channel flow. *Geophysical Research Letters*, 30(5), 1243. <https://doi.org/10.1029/2002GL016877>
- IGM (Instituto Geografico Militar) de Bolivia (2000). Digital Atlas of Bolivia, CD-ROM.
- Isacks, B. (1988). Uplift of the central Andean plateau and bending of the Bolivian orocline. *Journal of Geophysical Research*, 93(B4), 3211–3231. <https://doi.org/10.1029/JB093iB04p03211>
- Jacobshagen, V., Müller, J., Wemmer, K., Ahrendt, H., & Manutsoglu, E. (2002). Hercynian deformation and metamorphism in the Cordillera Oriental of southern Bolivia, central Andes. *Tectonophysics*, 345(1–4), 119–130. [https://doi.org/10.1016/S0040-1951\(01\)00209-8](https://doi.org/10.1016/S0040-1951(01)00209-8)
- James, D. E., & Sacks, S. (1999). Cenozoic formation of the central Andes: A geophysical perspective. *Society of Economic Geologists Special Publication*, 7, 1–25.
- Jordan, T. E., Isacks, B. L., Allmendinger, R. W., Brewer, J. A., Ramos, V. A., & Ando, C. J. (1983). Andean tectonics related to geometry of subducted Nazca Plate. *Geological Society of America Bulletin*, 94(3), 341–361. [https://doi.org/10.1130/0016-7606\(1983\)94<341:ARTTGO>2.0.CO;2](https://doi.org/10.1130/0016-7606(1983)94<341:ARTTGO>2.0.CO;2)
- Kay, R. W., & Kay, S. (1993). Delamination and delamination magmatism. *Tectonophysics*, 219(1–3), 177–189. [https://doi.org/10.1016/0040-1951\(93\)90295-U](https://doi.org/10.1016/0040-1951(93)90295-U)
- Kay, S. M., & Coira, B. L. (2009). Shallowing and steepening subduction zones, continental lithospheric loss, magmatism, and crustal flow under the Central Andean Altiplano-Puna Plateau. In S. M. Kay, V. A. Ramos, & W. R. Dickinson (Eds.), *Backbone of the Americas: Shallow subduction, plateau uplift, and ridge and terrane collision*: Geological Society of America Memoir (Vol. 204, ch. 11, pp. 229–259). [https://doi.org/10.1130/2009.1204\(11\)](https://doi.org/10.1130/2009.1204(11))
- Kay, S. M., Mpodozis, C., & Coira, B. (1999). Neogene magmatism, tectonism, and mineral deposits of the Central Andes (22°S to 33°S). In B. Skinner, et al. (Eds.), *Geology and Mineral Deposits of Central Andes: Society of Economic Geology, Special Publication* (Vol. 7, pp. 27–59).
- Kennan, L., Lamb, S., & Hoke, L. (1997). High-altitude paleosurfaces in the Bolivian Andes: Evidence for late Cenozoic surface uplift. In M. Widdowson (Ed.), *Paleosurfaces: Recognition, reconstruction and paleoenvironmental interpretation, Special Publication* (Vol. 120, pp. 307–323). London: Geological Society.
- Ketcham, R. a. (2005). Forward and inverse modeling of low-temperature thermochronometry data. *Reviews in Mineralogy and Geochemistry*, 58(1), 275–314. <https://doi.org/10.2138/rmg.2005.58.11>
- Ketcham, R. a., Carter, A., Donelick, R. a., Barbarand, J., & Hurford, A. J. (2007). Improved modeling of fission-track annealing in apatite. *American Mineralogist*, 92(5–6), 799–810. <https://doi.org/10.2138/am.2007.2281>
- Kley, J. (1996). Transition from basement-involved to thin-skinned thrusting in the Cordillera Oriental of southern Bolivia. *Tectonics*, 15(4), 763–775. <https://doi.org/10.1029/95TC03868>
- Kley, J., Gangui, A. H., & Kruger, D. (1996). Basement-involved blind thrusting in the eastern Cordillera Oriental, southern Bolivia: Evidence from cross-sectional balancing, gravimetric and magnetotelluric data. *Tectonophysics*, 259, 171–184.
- Kley, J., Muller, J., Tawackoli, S., Jacobshagen, V., & Manutsoglu, E. (1997). Pre-Andean and Andean-age deformation in the Eastern Cordillera of southern Bolivia. *Journal of South American Earth Sciences*, 10(1), 1–19. [https://doi.org/10.1016/S0895-9811\(97\)00001-1](https://doi.org/10.1016/S0895-9811(97)00001-1)
- Krystopowicz, N. J., & Currie, C. A. (2013). Crustal eclogitization and lithosphere delamination in orogens. *Earth and Planetary Science Letters*, 361, 195–207. <https://doi.org/10.1016/j.epsl.2012.09.056>
- Lamb, S. (2015). Cenozoic uplift of the central Andes in northern Chile and Bolivia- reconciling paleoaltimetry with geological evolution. *Canadian Journal of Earth Sciences*, 53, 1227–1245.
- Lamb, S., & Davis, P. (2003). Cenozoic climate change as a possible cause for the rise of the Andes. *Nature*, 425, 792–797.
- Lamb, S., & Hoke, L. (1997). Origin of the high plateau in the Central Andes, Bolivia, South America. *Tectonics*, 16, 623–649.
- Lease, R. O., & Ehlers, T. A. (2013). Incision into the eastern Andean Plateau during Pliocene cooling. *Science*, 341, 774–776. <https://doi.org/10.1126/science.1239132>
- Lease, R. O., Ehlers, T. A., & Enkelmann, E. (2016). Large along-strike variations in the onset of Subandean exhumation: Implications for Central Andean orogenic growth. *Earth and Planetary Science Letters*, 451, 62–76. <https://doi.org/10.1016/j.epsl.2016.07.004>
- Ludwig, K. R. (2012). *Isoplot 3.75: A geochronological toolkit for Microsoft Excel, Special Publication* (Vol. 5). Berkeley, CA: Berkeley Geochronology Center.
- Maloney, K. T., Clarke, G. L., Klepeis, K. A., & Quevedo, L. (2013). The late Jurassic to present evolution of the Andean margin: Drivers and the geological record. *Tectonics*, 32, 1049–1065. <https://doi.org/10.1002/tect.20067>
- McGroder, M. F., Lease, R. O., & Pearson, D. M. (2015). Along-strike variation in structural styles and hydrocarbon occurrences, Subandean fold-and-thrust belt and inner foreland, Colombia to Argentina. In P. G. Decelles, M. N. Ducea, B. Carrapa, & P. Kapp (Eds.), *Geodynamics of a Cordilleran orogenic system: The central Andes of Argentina and Northern Chile, Geological Society of America Memoir* (Vol. 212, pp. 79–113).
- McQuarrie, N. (2002). The kinematic history of the central Andean fold-thrust belt, Bolivia: Implications for building a high plateau. *Geological Society of America Bulletin*, 114(8), 950–963. [https://doi.org/10.1130/0016-7606\(2002\)114<0950](https://doi.org/10.1130/0016-7606(2002)114<0950)
- McQuarrie, N., Barnes, J. B., & Ehlers, T. A. (2008). Geometric, kinematic, and erosional history of the central Andean Plateau, Bolivia (15–17°S). *Tectonics*, 27, TC3007. <https://doi.org/10.1029/2006TC002054>
- McQuarrie, N., Ehlers, T. A., Barnes, J. B., & Meade, B. (2008). Temporal variation in climate and tectonic coupling in the central Andes. *Geology*, 36(12), 999–1002. <https://doi.org/10.1130/G25124A.1>
- McQuarrie, N., Horton, B. K., Zandt, G., Beck, S., & DeCelles, P. G. (2005). Lithospheric evolution of the Andean fold-thrust belt, Bolivia, and the origin of the central Andean plateau. *Tectonophysics*, 399(1–4), 15–37. <https://doi.org/10.1016/j.tecto.2004.12.013>

- Molnar, P., England, P., & Martinod, J. (1993). Mantle dynamics, uplift of the Tibetan Plateau, and Indian Monsoon. *Reviews of Geophysics*, 31(4), 357–396. <https://doi.org/10.1029/93RG02030>
- Molnar, P., & Garzione, C. N. (2007). Bounds on the viscosity coefficient of continental lithosphere from removal of mantle lithosphere beneath the Altiplano and Eastern Cordillera. *Tectonics*, 26, TC201. <https://doi.org/10.1029/2006TC001964>
- Mourgues, R., Lacoste, A., & Garibaldi, C. (2014). The Coulomb critical taper theory applied to gravitational instabilities. *Journal of Geophysical Research: Solid Earth*, 119, 754–765. <https://doi.org/10.1002/2013JB010359>
- Mulch, A., Uba, C. E., Strecker, M. R., Schoenberg, R., & Chamberlain, C. P. (2010). Late Miocene climate variability and surface elevation in the central Andes. *Earth and Planetary Science Letters*, 290(1–2), 173–182. <https://doi.org/10.1016/j.epsl.2009.12.019>
- Müller, J. P., Kley, J., & Jacobshagen, V. (2002). Structure and Cenozoic kinematics of the Eastern Cordillera, southern Bolivia (21°S). *Tectonics*, 21(5), 1037. <https://doi.org/10.1029/2001TC001340>
- Murray, K. E., Orme, D. A., & Reiners, P. W. (2014). Effects of U-Th-rich grain boundary phases on apatite helium ages. *Chemical Geology*, 390, 135–151. <https://doi.org/10.1016/j.chemgeo.2014.09.023>
- Myers, S. C., Beck, S., Zandt, G., & Wallace, T. (1998). Lithospheric-scale structure across the Bolivian Andes from tomographic images of velocity and attenuation for P and S waves. *Journal of Geophysical Research*, 103(B9), 21,233–21,252. <https://doi.org/10.1029/98JB00956>
- Oncken, O., Boutelier, D., Dresen, G., & Schemmann, K. (2012). Strain accumulation controls failure of a plate boundary zone: Linking deformation of the central Andes and lithosphere mechanics. *Geochemistry, Geophysics, Geosystems*, 13, Q12077. <https://doi.org/10.1029/2012GC004280>
- Oncken, O., Hindle, D., Kley, J., Elger, K., Victor, P., & Schemmann, K. (2006). Deformation of the central Andean upper plate system—Facts, fiction, and constraints for plateau models. In O. Oncken, et al. (Eds.), *The Andes—Active Subduction Orogeny* (pp. 3–27). Berlin: Springer-Verlag.
- O’Sullivan, P. B., & Parrish, R. R. (1995). The importance of apatite composition and single-grain ages when interpreting fission track data from plutonic rocks: A case study from the Coast Ranges, British Columbia. *Earth and Planetary Science Letters*, 132(1–4), 213–224. [https://doi.org/10.1016/0012-821X\(95\)00058-K](https://doi.org/10.1016/0012-821X(95)00058-K)
- Platt, J. P. (1986). Dynamics of orogenic wedges and the uplift of high-pressure metamorphic rocks. *Geological Society of America Bulletin*, 97(9), 1037–1053. [https://doi.org/10.1130/0016-7606\(1986\)97<1037:DOOWAT>2.0.CO;2](https://doi.org/10.1130/0016-7606(1986)97<1037:DOOWAT>2.0.CO;2)
- Pope, D. C., & Willett, S. D. (1998). Thermal-mechanical model for crustal thickening in the central Andes driven by ablative subduction. *Geology*, 26(6), 511–514. [https://doi.org/10.1130/0091-7613\(1998\)026<0511:TMMFCT>2.3.CO;2](https://doi.org/10.1130/0091-7613(1998)026<0511:TMMFCT>2.3.CO;2)
- Rak, A. J., McQuarrie, N., & Ehlers, T. A. (2017). Kinematics, exhumation, and sedimentation of the north central Andes (Bolivia): An integrated thermochronometer and thermokinematic modeling approach. *Tectonics*, 36, 2524–2554. <https://doi.org/10.1002/2016TC004440>
- Ramos, V. A. (2009). Anatomy and global context of the Andes: Main geologic features and the Andean orogenic cycle, in Kay, S. M., Ramos, V. A., and Dickinson, W. R., eds., *Backbone of the Americas: Shallow Subduction, Plateau Uplift, and Ridge and Terrane Collision*: Geological Society of America Memoir 204, ch. 2, pp. 31–65. [https://doi.org/10.1130/2009.1204\(02\)](https://doi.org/10.1130/2009.1204(02))
- Ramos, V. A., & Folguera, A. (2009). Andean flat-slab subduction through time. *Geological Society of London, Special Publication*, 327(1), 31–54. <https://doi.org/10.1144/SP327.3>
- Reiners, P. W., & Brandon, M. T. (2006). Using thermochronology to understand orogenic erosion. *Annual Review of Earth and Planetary Sciences*, 34(1), 419–466. <https://doi.org/10.1146/annurev.earth.34.031405.125202>
- Reiners, P. W., Ehlers, T. a., & Zeitler, P. K. (2005). Past, present, and future of thermochronology. *Reviews in Mineralogy and Geochemistry*, 58(1), 1–18. <https://doi.org/10.2138/rmg.2005.58.1>
- Reiners, P. W., Spell, T. L., Nicolescu, S., & Zanetti, K. A. (2004). Zircon (U-Th)/He thermochronometry: He diffusion and comparisons with <sup>40</sup>Ar/<sup>39</sup>Ar dating. *Geochimica et Cosmochimica Acta*, 68, 1857–1887. <https://doi.org/10.1016/j.gca.2003.10.021>
- Reiners, P. W., Thomson, S. N., Vernon, A., Willett, S. D., Quade, J., & Cavazza, W. (2015). Low-temperature thermochronologic trends across the central Andes, 21°S–28°S. In P. G. DeCelles, M. N. Ducea, B. Carrapa, & P. A. Kapp (Eds.), *Geodynamics of a Cordilleran orogenic system: The central Andes of Argentina and Northern Chile*, Geological Society of America Memoir (Vol. 212, pp. 215–249). [https://doi.org/10.1130/2015.1212\(12\)](https://doi.org/10.1130/2015.1212(12))
- Roe, G. H., & Brandon, M. T. (2011). Critical form and feedbacks in mountain-belt dynamics: Role of rheology as a tectonic governor. *Journal of Geophysical Research*, 116, B02101. <https://doi.org/10.1029/2009JB006571>
- Russo, R. M., & Silver, P. G. (1996). Cordillera formation, mantle dynamics, and the Wilson cycle. *Geology*, 24(6), 511–514. [https://doi.org/10.1130/0091-7613\(1996\)024<0511:CFMDAT>2.3.CO;2](https://doi.org/10.1130/0091-7613(1996)024<0511:CFMDAT>2.3.CO;2)
- Ryan, J., Beck, S., Zandt, G., Wagner, L., Minaya, E., & Tavera, H. (2016). Tectonophysics central Andean crustal structure from receiver function analysis. *Tectonophysics*, 682, 120–133. <https://doi.org/10.1016/j.tecto.2016.04.048>
- Saleeby, J., Ducea, M. N., & Clemens-Knott, D. (2003). Production and loss of high-density batholithic root, southern Sierra Nevada, California. *Tectonics*, 22(6), 1064. <https://doi.org/10.1029/2002TC001374>
- Schellart, W. P. (2008). Overriding plate shortening and extension above subduction zones: A parametric study to explain formation of the Andes Mountains. *Geological Society of America Bulletin*, 120(11–12), 1441–1454. <https://doi.org/10.1130/B26360.1>
- Schmitz, M., & Kley, J. (1997). The geometry of the central Andean backarc crust: Joint interpretation of cross-section balancing and seismic refraction data. *Journal of South American Earth Sciences*, 10, 99–110.
- Sempere, T. (1995). Phanerozoic evolution of Bolivia and adjacent regions. In A. J. Tankard, et al., (Eds.), *Petroleum basins of South America: American Association of Petroleum Geologists Memoir* (Vol. 62, pp. 207–230).
- Sempere, T., Butler, R. F., Richards, D. R., Marshall, L. G., Sharp, W., & Swisher, C. C. III (1997). Stratigraphy and chronology of Upper Cretaceous–lower Paleogene strata in Bolivia and northwest Argentina. *Geological Society of America Bulletin*, 109, 709–727. [https://doi.org/10.1130/0016-7606\(1997\)109<0709:SACOU>2.3.CO;2](https://doi.org/10.1130/0016-7606(1997)109<0709:SACOU>2.3.CO;2)
- Sempere, T., Carlier, G., Soler, P., Fornari, M., Carlotto, V., Jacay, J., et al. (2002). Late Permian–Middle Jurassic lithospheric thinning in Peru and Bolivia, and its bearing on Andean-age tectonics. *Tectonophysics*, 345(1–4), 153–181. [https://doi.org/10.1016/S0040-1951\(01\)00211-6](https://doi.org/10.1016/S0040-1951(01)00211-6)
- Servicio Nacional de Geologica y Tecnico de Minas and Yacimientos Petroliferos Fiscales Bolivianos (2003). Mapa geologico de Bolivia, scale 1:100,000, La Paz.
- Shuster, D. L., Flowers, R. M., & Farley, K. a. (2006). The influence of natural radiation damage on helium diffusion kinetics in apatite. *Earth and Planetary Science Letters*, 249(3–4), 148–161. <https://doi.org/10.1016/j.epsl.2006.07.028>
- Sobel, E. R., Hilley, G. E., & Strecker, M. R. (2003). Formation of internally drained contractional basins by aridity-limited bedrock incision. *Journal of Geophysical Research*, 108, 2344. <https://doi.org/10.1029/2002JB001883>
- Sobel, E. R., & Strecker, M. R. (2003). Uplift, exhumation and precipitation: Tectonic and climatic control of late Cenozoic landscape evolution in the northern Sierras Pampeanas, Argentina. *Basin Research*, 15(4), 431–451. <https://doi.org/10.1046/j.1365-2117.2003.00214.x>

- Springer, M., & Forster, A. (1998). Heat-flow density across the central Andean subduction zone. *Tectonophysics*, 291(1-4), 123–139. [https://doi.org/10.1016/S0040-1951\(98\)00035-3](https://doi.org/10.1016/S0040-1951(98)00035-3)
- Starck, D. (1995). Silurian-Jurassic stratigraphy and basin evolution of northwest Argentina. In A. J. Tankard, et al. (Eds.), *Petroleum Basins of South America, American Association of Petroleum Geologists Memoir* (Vol. 62, pp. 251–267).
- Stockli, D. F. (2005). Application of low-temperature thermochronometry to extensional tectonic settings. *Reviews in Mineralogy and Geochemistry*, 58(1), 411–448. <https://doi.org/10.2138/rmg.2005.58.16>
- Stockli, D. F., Surpless, B. E., & Dumitru, T. U. (2002). Thermochronological constraints on the timing and magnitude of Miocene and Pliocene extension in the central Wassuk Range, western Nevada. *Tectonics*, 21(4), 1028. <https://doi.org/10.1029/2001TC001295>
- Stolar, D. R., Willett, S. D., & Roe, G. H. (2006). Evolution of a critical orogen under various forcing scenarios: Findings from a numerical sand-box. In S. D. Willett, et al. (Eds.), *Tectonics, climate, and landscape evolution, Geological Society Special Paper* (Vol. 398, pp. 240–250).
- Strecker, M., Alonso, R. N., Bookhagen, B., Carrapa, B., Hilley, G. E., Sobel, E. R., & Trauth, M. H. (2007). Tectonics and climate of the southern central Andes. *Annual Review of Earth and Planetary Sciences*, 35(1), 747–787. <https://doi.org/10.1146/annurev.earth.35.031306.140158>
- Tankard, A., Ultiana, M. A., Welsink, H. J., Ramos, V. A., Turic, M., Franca, A. B., et al. (1995). Structural and tectonic controls of basin evolution in southwestern Gondwana during the Phanerozoic. In A. J. Tankard, et al. (Eds.), *Petroleum basins of South America, American Association of Petroleum Geologists Memoir* (Vol. 62, pp. 5–52).
- Tawackoli, S., Jacobshagen, V., Wemmer, K., and Andriessen, P., (1996). The eastern cordillera of southern Bolivia: A key region to the Andean backarc uplift and deformation history, in extended abstracts: Third International Symposium on Andean Geodynamics, St. Malo, France. ORSTOM, Paris, p. 505–508.
- Tawackoli, S. (1999). Andine Entwicklung der Ostkordillere in der Region Tupiza (Sudbolivien). Berlin. Geowiss. Abh., A, 203 (pp. 1–116).
- Thomson, S. N., Brandon, M. T., Reiners, P. W., Zattin, M., Isaacson, P. J., & Balestrieri, M. L. (2010). Thermochronologic evidence for orogen-parallel variability in wedge kinematics during extending convergent orogenesis of the northern Apennines, Italy. *Geological Society of America Bulletin*, 122(7-8), 1160–1179. <https://doi.org/10.1130/B26573.1>
- Uba, C. E., Heubeck, C., & Hulka, C. (2005). Facies analysis and basin architecture of the Neogene Subandean synorogenic wedge, southern Bolivia. *Sedimentary Geology*, 180(3-4), 91–123. <https://doi.org/10.1016/j.sedgeo.2005.06.013>
- Uba, C. E., Heubeck, C., & Hulka, C. (2006). Evolution of the late Cenozoic Chaco foreland basin, Southern Bolivia. *Basin Research*, 18(2), 145–170. <https://doi.org/10.1111/j.1365-2117.2006.00291.x>
- Uba, C. E., Kley, J., Strecker, M. R., & Schmitt, A. K. (2009). Unsteady evolution of the Bolivian Subandean thrust belt: The role of enhanced erosion and clastic wedge progradation. *Earth and Planetary Science Letters*, 281(3-4), 134–146. <https://doi.org/10.1016/j.epsl.2009.02.010>
- Uba, C. E., Strecker, M. R., & Schmitt, A. K. (2007). Increased sediment accumulation rates and climatic forcing in the central Andes during the late Miocene. *Geology*, 35(11), 979–982. <https://doi.org/10.1130/G224025A.1>
- Vermeech, P. (2009). RadialPlotter: A Java application for fission track, luminescence and other radial plots. *Radiation Measurements*, 44(4), 409–410. <https://doi.org/10.1016/j.radmeas.2009.05.003>
- Wells, M. L., Hoisch, T. D., Cruz-Urbe, A. M., & Vervoort, J. D. (2012). Geodynamics of synconvergent extension and tectonic mode switching: Constraints from the Sevier-Laramide orogen. *Tectonics*, 31, TC1002. <https://doi.org/10.1029/2011TC002913>
- Welsink, H. J., Martinez, E., Aranibar, O., & Jaradilla, J. (1995). Structural inversion of a Cretaceous rift basin, southern Altiplano, Bolivia. In A. J. Tankard, et al. (Eds.), *Petroleum basins of South America, American Association of Petroleum Geologists Memoir* (Vol. 62, pp. 305–324).
- Whipple, K. X. (2009). The influence of climate on the tectonic evolution of mountain belts. *Nature Geoscience*, 2(2), 97–104. <https://doi.org/10.1038/NCEO413>
- Whipple, K. X., & Meade, B. J. (2006). Orogen response to changes in climatic and tectonic forcing. *Earth and Planetary Science Letters*, 243(1-2), 218–228. <https://doi.org/10.1016/j.epsl.2005.12.022>
- Wigger, P., Schmitz, M., Araneda, M., Asch, G., Baldzuhn, S., Giese, P., et al. (1994). Variation in the crustal structure of the southern Central Andes deduced from seismic refraction investigations. In L. Reutter, et al. (Eds.), *Tectonics of the Southern Central Andes* (pp. 23–48). New York: Springer-Verlag. [https://doi.org/10.1007/978-3-642-77353-2\\_2](https://doi.org/10.1007/978-3-642-77353-2_2)
- Willett, S., & Brandon, M. (2002). On steady states in mountain belt. *Geology*, 30(2), 175–178. [https://doi.org/10.1130/0091-7613\(2002\)030<0175:OSSIMB>2.0.CO;2](https://doi.org/10.1130/0091-7613(2002)030<0175:OSSIMB>2.0.CO;2)
- Willett, S. D. (1999). Orogeny and orography: The effects of erosion on the structure of mountain belts. *Journal of Geophysical Research*, 104, 28957. <https://doi.org/10.1029/1999JB900248>
- Wojtal, S., & Mitra, G. (1986). Strain hardening and strain softening in fault zones from foreland thrusts. *Geological Society of America Bulletin*, 97(6), 674–687. [https://doi.org/10.1130/0016-7606\(1986\)97<674:SHASSI>2.0.CO;2](https://doi.org/10.1130/0016-7606(1986)97<674:SHASSI>2.0.CO;2)
- Wolf, R. A., Farley, K. A., & Kass, D. M. (1998). Modeling of the temperature sensitivity of the apatite (U-Th)/He thermochronometer. *Chemical Geology*, 148(1-2), 105–114. [https://doi.org/10.1016/S0009-2541\(98\)00024-2](https://doi.org/10.1016/S0009-2541(98)00024-2)
- Wolfe, M. R., & Stockli, D. F. (2010). Zircon (U-Th)/He thermochronometry in the KTB drill hole, Germany, and its implications for bulk He diffusion kinetics in zircon. *Earth and Planetary Science Letters*, 295(1-2), 69–82. <https://doi.org/10.1016/j.epsl.2010.03.025>
- Yamada, R., Murakami, M., & Tagami, T. (2007). Statistical modelling of annealing kinetics of fission tracks in zircon: Reassessment of laboratory experiments. *Chemical Geology*, 236(1-2), 75–91. <https://doi.org/10.1016/j.chemgeo.2006.09.002>